Dark matter effect on black hole accretion disks

D. Pugliese and Z. Stuchlík

Research Centre for Theoretical Physics and Astrophysics, Institute of Physics, Silesian University in Opava, Bezručovo náměstí 13, CZ-74601 Opava, Czech Republic

(Received 11 May 2022; accepted 21 November 2022; published 23 December 2022)

Comparing different dark matter (DM) models, we explore the DM influence on black hole (BH) accretion disk physics, considering corotating and counterrotating thick accretion tori orbiting a central spinning BH. Our results identify accretion onto a central BH as a good indicator of DM presence, signaling possible DM tracers in accretion physics. We analyze accretion around a spinning BH immersed in perfect-fluid dark matter, cold dark matter and scalar field dark matter. Our investigation addresses observational evidence of distinctive DM effects on toroidal accretion disks and protojet configurations, proving that BH accretion tori immersed in DM can present characteristics, such as interdisk cusp or double tori, which have usually been considered as tracers for superspinars and naked singularity attractors. Therefore, in this context DM influence on the BH geometry could manifest as superspinar mimickers. DM also affects the central spinning attractor energetics associated with accretion physics, and its influence on accretion disks can be searched for in a variation of the central BH energetics as an increase of the mass accretion rates.

DOI: 10.1103/PhysRevD.106.124034

I. INTRODUCTION

In this work we study the dark matter (DM) influence on black hole (BH) accretion disk physics, investigating the accretion disk morphology for corotating and counterrotating geometrically thick accretion tori orbiting a central spinning BH. Comparing three different DM models, our analysis points out possible observational evidence of distinctive DM effects on the accretion disks, which can be traces of DM presence. Our investigation does not cover all the admissible parametric DM values for the deformed metrics, but, taking into account constraints formerly obtained by the study of orbits, DM-BH shadows, and emission spectra, we perform a comparative analysis of the DM models and an investigation of the constraints imposed on the accretion disks aimed at further restricting the parameter range and pointing out possible marks of DM in some accretion features. From a methodological viewpoint we take advantage of the axial symmetry of DM metrics, studying fully general relativistic models of stationary toroidal orbiting configurations.

The physics of accretion disks around BHs and supermassive black holes (SMBHs), hosted in quasars and active galactic nuclei, powers the most energetic processes of our Universe, which are often accompanied by an ejection of matter in jetlike structures with extremely large radiative energy output. We investigate the DM effects on these aspects, focusing on SMBH at the center of galaxies and the accretion disks empowering the emissions. We analyze in particular the limiting situation of static (and spherically symmetric) background (with spin parameter $a = 0$) and the DM deformation on the Kerr extreme BH spacetime (with spin value $a = M$), seeing significant qualitative detectable variations with respect to the standard vacuum BH case. Many astrophysical observations lead to a SMBH hosted at the Galactic Center embedded in a DM halo, and in metric models considered here the central BH is surrounded by a DM envelope that modifies the geometry around the BH, not interacting directly with the accreting matter or its radiation.

More generally, there is a large amount of observational evidence of the presence of some kind of DM component in our Universe, for example, from the galactic rotation curves and galaxy cluster dynamics. However, within the variety of different observations indicating a DM presence, there is no single metric that encompasses all the DM effects in a single model and that could also explain the absence of DM observed at different scales.[1] In this work we consider a spinning BH immersed in perfect-fluid DM (PFDM) [4–7], cold dark matter (CDM), and scalar field dark matter (SFDM) [8,9].

These DM models have been extensively studied in the recent literature. The PFDM model was considered in [5]

[1]An important issue is then the mass (or space) scale when DM effects became significant. For example, DM results missing in some galaxies (e.g., AGC 114905 [1,2]), and an explanation for this situation is that the Galaxy may have been stripped of dark matter from nearby massive galaxies, while the DM presence in the Solar System is still an open problem [3].

and the effects of PFDM on particle motion around a static BH in an external magnetic field were studied in [10]. The shadow of the spinning BH in PFDM was studied in [4], whereas in [6] geodesic motion in PFDM Kerr and Kerr–anti–de Sitter/de Sitter BH were studied; see also [7]. For studies of the geodesic in the Kerr–de Sitter spacetimes, see [11–15]. In [16] superradiance and the stability of Kerr DM enclosed by anisotropic fluid matter were studied. Spinning BH solutions with quintessential energy were discussed in [17]. In [8] a BH in a DM halo was considered. Rotating black holes with an anisotropic matter field was considered in [18], while in [9] there is a discussion of the BH shadow of Sgr A* in a DM halo. Superradiance and instabilities in BHs surrounded by anisotropic fluids were considered in [19]. Galactic dark matter in the phantom field model was considered in [20]. The case of rotating (Kerr) naked singularities was treated in [21–24]. Here we focus on the influence of DM on BHs governing toroidal accretion structures.

There is an extensive literature exploring the DM effects on the BH and BH accretion physics. Since DM influences different aspects of the singularity, from the characteristics of the horizon (for example, it can manifest itself in the BH shadows) to the energetics properties of the surrounding matter, there are various assessments of the DM effects and parameter constraints on the models describing DM presence around BHs. In [25], for example, DM clouds of axions around BHs were studied with superradiant instabilities and accretion, which could manifest on the gravitational-wave signal induced by a small compact object in the field of the central BH; see also [26,27]. More recently [28] the formation of SMBHs at high redshifts was studied in connection with ultralight DM; see also [29,30] for a growth of accretion driven scalar DM hair around a Kerr BH. The DM effect on the quasinormal modes of massless scalar field and electromagnetic field perturbations in a BH spacetime surrounded by PFDM was considered in [31]. An analysis of DM in the M87 core in relation to BH shadow effects was presented in [32] (see also [33]), and shadows of a Sgr A* BH surrounded by a superfluid DM halo was studied in [34], and the shadow from a charged rotating BH in the presence of PFDM is explored in [35].

The DM candidates are many, including string and brane theory effects, boson clouds, hypothetical new particles, primordial BHs, and alternative theories of gravity.[2] From an observational viewpoint, dark matter can be detected from the products of its decay or annihilation in cosmic rays, gamma rays, neutrinos, or even gravitons (see also [37]), and gravitational-wave and neutrino astronomy can then open different windows into the DM analysis.[3] DM comprehension, particularly that focused on subgalactic DM halos, is also a goal of the Webb Telescope.[4]

Nevertheless, despite the variety of DM models, the standard cosmological model is in fact the ΛCDM, which includes a cosmological constant (Λ) (with negative pressure) encoding dark energy in empty space (or vacuum energy) that explains the Universe accelerating expansion. (In this scenario the effects of the cosmological constant are also treated as quintessence.[5]) Polytropic models of DM halos in ΛCDM cosmology were individuated in [45]. In this model, the DM velocity is less than the speed of light (in this respect neutrinos component are excluded, as they are nonbaryonic but not necessarily cold), and it is dissipationless, as it is not cooled by radiating photons. CDM may be constituted by hypothetical weakly interacting massive particles, primordial BHs, or axions.

Although considered a DM standard model, CDM is not exempt from various problems, emerging, for example, from the observations of galaxies and galaxy clusters and clusterization emerging from rotation curves and morphological studies (such as the cuspy halo problem). There is also a more general problem in describing the effects and presence of DM at large and small scales. The CDM model therefore collides with small-scale structure observations. For all these reasons the search for alternative DM models is still an open challenge, and in this respect the SFDM model seems to adapt to both large-scale and small-scale structure observations, while the PFDM seems capable of explaining the asymptotically flat rotation velocity characterizing spiral galaxies.

In this analysis we study geometrically thick accretion disk models, Polish doughnuts (PDs), which orbit the central attractor and whose center coincides with the equatorial plane of the central axisymmetric attractor [46–50]. These thick accretion tori are characterized by very high (super-Eddington) accretion rates and high optical depth. Torus morphology and stability are essentially governed by the pressure gradients on the equatorial plane [46]. The thin (Keplerian) disks can be considered PD limiting configurations regulated by the background geodesic structure. The DM background metric has a characteristic geodetic structure constituting the first major constraint on accretion physics. The tori described by purely hydrodynamic (barotropic) models are governed

[2]Dark matter was also explained with diffuse clouds of scalar bosons interacting with gravity and gravitational waves. However, recent results in [36] set constrains on this hypothesis, showing that there are no young scalar boson clouds in our Galaxy.

[3]Concerning possible DM constituents and their presence in our Galaxy, we mention that the DM Milky Way has been recently studied in [38,39], whereas DM and primordial BHs are studied in [40,41]. Constraints on DM rule out BHs constituting only a very small possible fraction of dark matter. Finally, a hypothesis suggesting that antimatter and DM are linked was recently studied in [42], posing limits on the interaction of antiprotons with axionlike DM; see also [43].

[4]See https://jwst.nasa.gov.

[5]See [44] for a recent analysis constraining the fraction of early dark energy that was present in the early stages of the Universe.

by the equipressure surfaces that can be closed, giving stable equilibrium configurations, or open, giving unstable, jetlike (protojet) structures caused by the relativistic instability due to the Paczynski mechanism, where the effects of strong gravitational fields are dominant[6] with respect to the dissipative ones and predominant to determine the unstable phases of the systems [53–60].

Many features of the torus dynamics and morphology, like their thickness, their stretching in the equatorial plane, and the location of the tori, are predominantly determined by the geometric properties of spacetime via a fluid effective potential function. Consequently, in models where DM is geometrized as a metric deformation, DM has a clear impact on the torus structure, modifying the fluid effective potential. The gradients of the effective potential on the torus equatorial and symmetry plane regulate the pressure gradient of the fluid in the Euler law governing dynamics of the perfect fluid [50]. The special case of cusped equipotential surfaces is related to the accretion phase in the central attractor [46,47,50,59,61]. The outflow of matter through the cusp occurs due to an instability in the balance of the gravitational and inertial forces and the pressure gradients in the fluid, i.e., by the so-called Paczynski mechanism of violation of mechanical equilibrium of the tori [47].

DM affects cusp formation and cusp location with respect to the central singularity, modifying the disk accretion throat, constraining the thickness of the accretionary flow and the maximum amount of matter swallowed by the central BH. Consequently, DM will influence the energetic characteristics of the BH in accretion and the disk characteristics, such as accretion rates and cusp luminosity [62–64].

The article is organized as follows: Thick disks in axially symmetric spacetimes are discussed in Sec. II. The Kerr metric is introduced in Sec. II A. The Polish doughnut torus models are detailed in Sec. II B. The fluid effective potential is the subject of Sec. II B 1. The extended geodesic structure constraining the torus modes is explored in Sec. II B 2. Dark matter models are discussed in Sec. III. In Sec. III A perfect-fluid dark matter is considered. Cold and scalar field dark matter models are studied in Sec. III B. Discussion and conclusions follow in Sec. IV.

[6]The timescale of the dynamical processes (regulated by the gravitational and inertial forces) is much lower than the timescale of the thermal ones (heating and cooling processes, radiation), which is lower than the timescale of the viscous processes. The entropy is constant along the flow and, according to the von Zeipel condition, the surfaces of constant angular velocity Ω and of constant specific angular momentum ℓ coincide. This implies that the rotation law $\ell = \ell(\Omega)$ is independent of the equation of state [51,52].

II. THICK DISKS IN AXIALLY SYMMETRIC SPACETIMES

We study geometrically thick tori in axially symmetric DM-BH spacetimes, considered as a DM-induced deformation of the Kerr geometry. Therefore, it is useful here to review the properties of the Kerr metric and the construction of tori in this geometry. More specifically, in Sec. II A the Kerr metric is introduced, while the Polish doughnut torus models are discussed in Sec. II B.

A. The Kerr metric

The Kerr metric is an axially symmetric, asymptotically flat, vacuum exact solution of the Einstein equation describing the spacetime of central spinning compact object. According to the metric parameter values (dimensionless spin a/M), the Kerr metric describes naked singularities (NSs) for $a > M$ and BHs for $a \in [0, M]$. The Kerr BH geometry has the limiting static solution of Schwarzschild for $a = 0$ and the extreme Kerr BH spacetime for $a = M$.

In the Boyer-Lindquist (BL) coordinates $\{t, r, \theta, \phi\}$, the metric tensor reads[7]

$$\begin{aligned} ds^2 = &-\left(1 - \frac{2Mr}{\Sigma}\right)dt^2 + \frac{\Sigma}{\Delta}dr^2 + \Sigma d\theta^2 \\ &+ \left[(r^2 + a^2) + \frac{2Mra^2}{\Sigma}\sin^2\theta\right]\sin^2\theta d\phi^2 \\ &- \frac{4rMa}{\Sigma}\sin^2\theta dt d\phi, \end{aligned} \tag{1}$$

where

$$\Delta \equiv a^2 + r^2 - 2rM, \quad \Sigma \equiv a^2(1-\sigma) + r^2, \quad \sigma \equiv \sin^2\theta, \tag{2}$$

with $G = c = 1$. The horizons $r_- < r_+$ are given, respectively, by

$$r_\pm \equiv M \pm \sqrt{M^2 - a^2}, \tag{3}$$

and the horizons can be found[8] by solving the equation $a = a_\pm \equiv \sqrt{r(2M - r)}$ for $r \in [0, 2M]$. The outer and inner stationary limits $r_e^\pm$ (ergosurfaces) (solutions of $g_{tt} = 0$) are, respectively,

[7]We adopt the geometrical units $c = 1 = G$ and the $(-,+,+,+)$ signature; latin indices run in $\{0,1,2,3\}$. The radius r has the unit of mass $[M]$ and the angular momentum has units of $[M]^2$. The velocities are $[u^t] = [u^r] = 1$ and $[u^\phi] = [u^\theta] = [M]^{-1}$, with $[u^\phi/u^t] = [M]^{-1}$ and $[u_\phi/u_t] = [M]$. For the sake of convenience, we always consider the dimensionless energy and effective potential $[V_{\rm eff}] = 1$ and an angular momentum per unit of mass $[L]/[M] = [M]$.

[8]Quantities $a_\pm$ and $a_e^\pm$ turn out to be very useful in the comparison of DM solutions of Sec. III with respect to Kerr solutions in the absence of DM.

$$r_\epsilon^\pm \equiv M \pm \sqrt{M^2 - a^2(1-\sigma)}. \tag{4}$$

The ergosurfaces can be found by solving the equation $a = a_\epsilon^\pm \equiv a_\pm/\sqrt{1-\sigma}$ (for $\sigma \neq 1$), where $r_+ < r_\epsilon^+$ on $\theta \neq 0$ and $r_\epsilon^+ = 2M$ in the equatorial plane $\theta = \pi/2$ ($\sigma = 1$). Static observers with a four-velocity $\dot\theta = \dot r = \dot\phi = 0$ [where $\dot q$ indicates the derivative of any quantity q with respect to the proper time (for timelike particles) or a properly defined affine parameter for lightlike orbits] cannot exist inside the (outer) ergoregion,[9] but trajectories $\dot r \geq 0$, including particles crossing the stationary limit and escaping outside the region $r \geq r_\epsilon^+$, are possible.

The constants of the geodesic motions are

$$\mathcal{E} = -(g_{t\phi}\dot\phi + g_{tt}\dot t), \qquad \mathcal{L} = g_{\phi\phi}\dot\phi + g_{t\phi}\dot t, \qquad g_{ab}u^a u^b = -\mu^2, \tag{5}$$

with[10] $u^a \equiv \{\dot t, \dot r, \dot\theta, \dot\phi\}$. In Eqs. (5) the quantities $\mathcal{E}$ and $\mathcal{L}$ represent the total energy and momentum of the test particle coming from radial infinity, as measured by a static observer at infinity.

The relativistic angular velocity and the specific angular momentum are

$$\Omega \equiv \frac{u^\phi}{u^t} = -\frac{\mathcal{E}g_{\phi t} + g_{tt}\mathcal{L}}{\mathcal{E}g_{\phi\phi} + g_{\phi t}\mathcal{L}} = -\frac{g_{t\phi} + g_{tt}\ell}{g_{\phi\phi} + g_{t\phi}\ell},$$
$$\ell \equiv \frac{\mathcal{L}}{\mathcal{E}} = -\frac{u_\phi}{u_t} = -\frac{g_{\phi\phi}u^\phi + g_{\phi t}u^t}{g_{tt}u^t + g_{\phi t}u^\phi} = -\frac{g_{t\phi} + g_{\phi\phi}\Omega}{g_{tt} + g_{t\phi}\Omega}, \tag{6}$$

respectively. The sign of $\mathcal{L}(\ell)$ defines the corotation/counterrotation of the particles (fluid). The DM models are axis symmetric and stationary and we similarly define the notion of corotating and counterrotating motions.

B. Geometrically thick tori: The Polish doughnut models

Our analysis specializes on the PD tori, general relativistic hydrodynamic (GRHD) toroidal configurations centered on the central BH equatorial plane, which is coincident with the torus equatorial symmetry plane. These toroidal models are well known and are used in different contexts. They are analytic and general relativistic models defined and integrable in axis-symmetric spacetimes, where the results known as the von Zeipel theorem hold, ensuring the integration condition on the equations for the fluid. For this reason we apply these results to the stationary DM metric models here.[11]

Tori are composed of one particle-species perfect fluid, where

$$T_{ab} = (\varrho + p)u_a u_b + p g_{ab} \tag{7}$$

is the fluid energy-momentum tensor and ϱ and p are the total energy density and pressure, respectively, as measured by an observer moving with the fluid. The timelike flow vector field u^a denotes the fluid four-velocity. The fluid dynamics is described by the continuity equation and the Euler equation, respectively,

$$u^a\nabla_a\varrho + (p+\varrho)\nabla^a u_a = 0, \quad (p+\varrho)u^a\nabla_a u^c + h^{bc}\nabla_b p = 0, \tag{8}$$

where the projection tensor $h_{ab} = g_{ab} + u_a u_b$ and $\nabla_a g_{bc} = 0$.

We assume a barotropic equation of state (EOS) $p = p(\varrho)$ and that the stationary and axially symmetric matter distribution moves in circular trajectories. We investigate fluid toroidal configurations defined by the constraint $u^r = 0$. Similarly to the test particle circular motion, no motion is assumed for the toroidal fluid in the θ angular direction, i.e. there is $u^\theta = 0$. Because of these symmetries, the continuity equation is identically satisfied and the orbiting configurations are regulated by the Euler equation for the pressure p only, which can be written as

$$\frac{\partial_a p}{\varrho + p} = -\partial_a W + \frac{\Omega\partial_a\ell}{1-\Omega\ell}, \quad \text{with } W \equiv \ln V_{\text{eff}} \text{ and } V_{\text{eff}} = u_t, \tag{9}$$

where V_{eff} is the torus effective potential. Tori are regulated by the balance of the hydrostatic and centrifugal factors due to the fluid rotation and by the curvature effects of the background, which are encoded in the effective potential function V_{eff}.

Assuming that the fluid is characterized by the specific angular momentum ℓ constant (see also the discussion in [51]), we consider the equation for W: $\ln(V_{\text{eff}}) = \text{c} =$

[9]The ergoregion is the range $[r_\epsilon^-, r_\epsilon^+]$ (where $r_\epsilon^\pm$ are functions of the plane $\sigma \in [0, 1]$). Here we often intend the outer ergoregion (or simply ergoregion) in the BH spacetimes as the region $]r_+, r_\epsilon^+]$. Then, on the equatorial planes in the Kerr spacetime, $r_\epsilon^- = 0$ and the outer ergosurface is $r_\epsilon^+ = 2M$.

[10]The other constant of geodesic motion of the Kerr metric is the Carter constant $\mathcal{Q} = (\cos\theta)^2[a^2(\mu^2 - \mathcal{E}^2) + (\frac{\mathcal{L}}{\sin\theta})^2] + (g_{\theta\theta}\dot\theta)^2$. In this work, where tori share the symmetry plane with the equatorial plane of the central BH, this constant is irrelevant.

[11]The toroids are constant pressure surfaces whose construction in the axis-symmetric spacetimes is based on the application of the von Zeipel theorem, in which the surfaces of the constant angular velocity Ω and the constant specific angular momentum ℓ coincide and the toroid rotation law $\ell = \ell(\Omega)$ is independent of the details of the equation of state. More precisely, the von Zeipel theorem reduces to an integrability condition on the Euler equation, in the case of barotropic fluids, where $\ell = \ell(\Omega)$. Consequently, in the geometrically thick disks the functional form of the angular momentum and entropy distribution during the evolution of dynamical processes depends on the initial conditions of the system and not on the details of the dissipative processes [57].

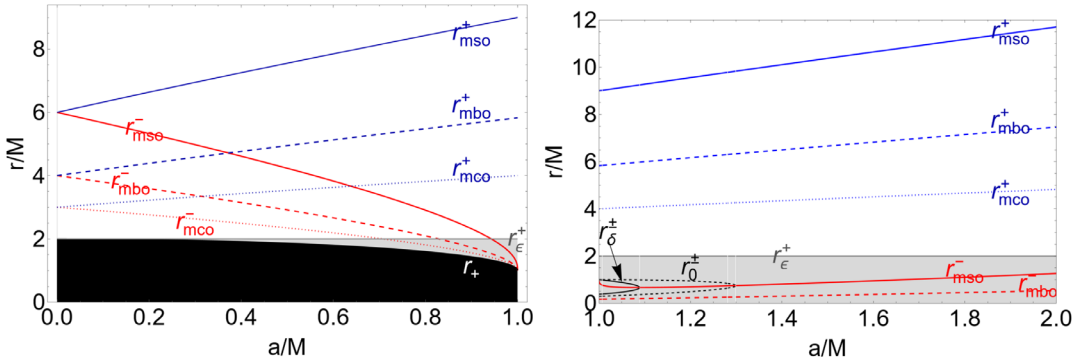

FIG. 1. Geodesic equatorial circular structure of the Kerr geometry for spin (left panel) $a \in [0, M]$ and (right panel) $a > M$, for corotating [(−); red curves] and counterrotating [(+); blue curves] orbits. Marginally stable orbits (*mso*) are displayed as solid curves, marginally bounded orbits (*mbo*) are shown as dashed curves, and marginally circular orbits $r^\pm_{mco}$ (which are also photon circular orbits) are displayed as dotted curves. [Note that for $a > M$ there is no last corotating circular orbit (i.e., $r^-_{mco} = 0$).] Radius r_+ is the outer horizon, and r^+_ϵ is the outer ergosurface on the equatorial plane. The black region is $r < r_+$, and the gray region is $r \in [r_+, r^+_\epsilon]$ for Kerr BHs and $r \in [0, r^+_\epsilon]$ for Kerr NSs. On radii $r^\pm_0$ (black dashed curve, right panel) $\mathcal{L} = 0$ (where $\mathcal{L}$ is the test particle angular momentum), and on radii $r^\pm_\delta$ (black curve, right panel) $\mathcal{E} = 0$ (where $\mathcal{E}$ is the test particle energy).

constant or $V_{\rm eff} = K =$ constant. By setting $\ell =$ constant as a torus parameter, the maximum density points in the disk, the pressure gradients (from the Euler equation), are determined by the gradients of the torus effective potential function.[12] The maximum points of the torus effective potential as a function of the radial coordinate provide the minimum points of pressure, where fluid particles are free on unstable circular geodetic orbits.

1. The fluid effective potential

The fluid effective potential (9) is, explicitly [57,66],

$$V^2_{\rm eff} = \left(\frac{\mathcal{E}}{\mu}\right)^2 = \frac{g^2_{t\phi} - g_{\phi\phi} g_{tt}}{g_{\phi\phi} + 2 g_{t\phi}\ell + g_{tt}\ell^2}. \tag{10}$$

The extremes of the pressure are regulated by the angular momentum distributions $\ell^\pm : \partial_r V_{\rm eff} = 0$ on the equatorial plane $\theta = \pi/2$ for corotating (−) and counterrotating (+) fluids, respectively.[13]

The torus cusp $r_\times$ is the minimum point of pressure and density in the torus corresponding to the maximum point of the fluid effective potential. The torus center $r_{\rm center}$ is the maximum point of pressure and density in the torus corresponding to the minimum point of the fluid effective potential. At the cusp ($r \le r_\times$) the fluid may be considered pressure-free. Fluid effective potential defines the function $K(r) = V_{\rm eff}(\ell(r))$. Cusped tori have a parameter in the open ranges[14] $K = K_\times \equiv K(r_\times) \in]K_{\rm center}, 1[\subset]K_{mso}, 1[$, where $K_{\rm center} \equiv K(r_{\rm center})$. [We adopt the notation $q_\bullet \equiv q(r_\bullet)$ for any quantity q evaluated on a radius $r_\bullet$.]

2. Extended geodesic structure and notable radii

The geometry equatorial circular geodesic structure constrains the accretion disk physics governing in the PD model, the torus cusps, and the center locations. In the Kerr geometry the geodesic structure constitutes the marginally circular orbit for timelike particles $r^\pm_{mso}$, which is also a photon circular orbit $r^\pm_{mco} \equiv r^\pm_\gamma$, the marginally bounded orbit $r^\pm_{mbo}$, and the marginally stable circular orbit $r^\pm_{mso}$ [see Fig. 1].[15] Radii $\{r^\pm_{mso}, r^\pm_{mbo}, r^\pm_{mco}\}$ constrain the location of the torus cusps (inner edges) with fluid specific angular momentum $\ell = \ell^\pm$, respectively,

[12]The procedure adopted here borrows from the Boyer theory on the equipressure surfaces applied to a thick torus [57,65]. The Boyer surface tori are given by the surfaces of constant pressure.

[13]Note that, in the test particle analysis and accretion torus models for slowly spinning NSs ($a \in]M, 1.29M[$), there are circular geodesic orbits with $(\mathcal{E} < 0, \mathcal{L} < 0)$ and $(\mathcal{E} > 0, \mathcal{L} < 0)$ on the equatorial plane of the ergoregion; see Fig. 1. These solutions correspond to the relativistic angular velocity (the Keplerian velocity with respect to static observers at infinity $\Omega = d\phi/dt$) $\Omega > 0$. Therefore, in this sense, they are all corotating with respect to the static observers at infinity, but they can be counterrotating according to $\mathcal{L} < 0$ and $\ell < 0$ or counterrotating according to $\mathcal{L} < 0$ but corotating according to $\ell > 0$. There can also be orbits with $\ell = \Omega = 0$; see, for example, [22,67–72]. This possibility has not been discussed in the analysis of DM models.

[14]The notation is as follows: the (closed) interval between quantities q_l and q_r, including q_l and q_r, is denoted as $[q_l, q_r] = \{q \in \mathbb{R} : q_l \le q \le q_r\}$, while the notation $]q_l, q_r[= \{q \in \mathbb{R} : q_l < q < q_r\}$ denotes the open interval. Similarly, $]q_l, q_r] = \{q \in \mathbb{R} : q_l < q \le q_r\}$ and $[q_l, q_r[= \{q \in \mathbb{R} : q_l \le q < q_r\}$.

[15]In the Kerr spacetime $r^\pm_{mco}$ is the marginal circular orbit (a photon circular orbit) where timelike circular orbits can fill the spacetime region $r > r^\pm_{mco}$. Stable circular orbits are in $r > r^\pm_{mso}$ for counterrotating and corotating test particles, respectively. The marginal bounded circular orbit is $r^\pm_{mbo}$, where $\mathcal{E}^\pm(r^\pm_{mbo}) = 1$. More details and the exact forms of these radii can be found, for example, in [68].

$$\text{where } r^{\pm}_{mco} < r^{\pm}_{mbo} < r^{\pm}_{mso} < r^{\pm}_{(mbo)} < r^{\pm}_{(mco)}, \tag{11}$$

where we also introduced the radii $(r^{\pm}_{(mbo)}, r^{\pm}_{(mco)})$, which are defined as

$$r^{\pm}_{(mbo)}: \ell^{\pm}(r^{\pm}_{mbo}) = \ell^{\pm}(r^{\pm}_{(mbo)}) \equiv \ell^{\pm}_{mbo},$$
$$r^{\pm}_{(mco)}: \ell^{\pm}(r^{\pm}_{mco}) = \ell^{\pm}(r^{\pm}_{(mco)}) \equiv \ell^{\pm}_{mco},$$

which is significant since the radii govern the location of the torus centers. More precisely, the ranges $(\mathbf{L_1}, \mathbf{L_2}, \mathbf{L_3})$ of the fluid specific angular momentum ℓ govern the torus topology, according to the geodesic structure of Eq. (11), as follows.

$\mathbf{L_1}$.—For $\ell \in \mathbf{L_1}$ there are quiescent (i.e., not cusped) and cusped tori where there is $\mp \mathbf{L_1}^{\pm} \equiv [\mp \ell^{\pm}_{mso}, \mp \ell^{\pm}_{mbo}[$. The cusp is $r^{\pm}_{\times} \in]r^{\pm}_{mbo}, r^{\pm}_{mso}]$ (with $K^{\pm}_{\times} < 1$) and the center with maximum pressure in $r^{\pm}_{\text{center}} \in]r^{\pm}_{mso}, r^{\pm}_{(mbo)}]$.

$\mathbf{L_2}$.—For $\ell \in \mathbf{L_2}$ there are quiescent tori and protojets (open configurations) where $\mp \mathbf{L_2}^{\pm} \equiv [\mp \ell^{\pm}_{mbo}, \mp \ell^{\pm}_{mco}[$. The cusp $r^{\pm}_{\times} \in]r^{\pm}_{mco}, r^{\pm}_{mbo}]$ is associated with the protojets, with $K_{\times} > 1$, and the center with maximum pressure is in $r^{\pm}_{\text{center}} \in]r^{\pm}_{(mbo)}, r^{\pm}_{(mco)}]$. Protojets are associated with (noncollimated) open structures, with matter funnels along the BH rotational axis; see [58,73–75].

$\mathbf{L_3}$.—For $\ell \in \mathbf{L_3}$ there are only quiescent tori where $\mp \mathbf{L_3}^{\pm} \equiv \mp \ell \geq \mp \ell^{\pm}_{mco}$ and the torus center is at $r^{\pm}_{\text{center}} > r^{\pm}_{(mco)}$. In the metric models that we consider, the DM affects the orbiting fluids modifying the Kerr axially symmetric geometry and the fluid effective potential; see also [76]. Therefore, we study the radii limiting the torus construction, defined through the fluid effective potential for the geometries modified by the DM. More precisely, we identify the marginally circular orbit $r^{\pm}_{mco}$ as the radius $r^{\pm}_{mco}: K^{\pm}(r) = \infty$, the marginally bounded orbit defined by $r^{\pm}_{mbo}: K^{\pm}(r) = 1$ (asymptotically flat spacetimes), and the marginally stable orbits $r^{\pm}_{mso}: \partial_r \ell^{\pm} = 0$.

The orbiting fluid is governed by the geodesic structure of the considered spacetime. The tori are specified by the profile of the distribution of the specific angular momentum of the orbiting matter (in the equator) and its relation to the radial profile of the specific angular momentum of equatorial circular geodesics. The so-called Keplerian distribution of the circular geodesic angular momentum related to a given spacetime is generally given by the relation

$$\ell = \ell_K \equiv \frac{\Phi_o \mp \sqrt{\Phi \Phi^2_{(-)}}}{\Phi_\star}, \quad \text{where } \Phi_{(\mp)} \equiv g^2_{t\phi} \mp g_{tt} g_{\phi\phi}, \qquad \Phi \equiv (g'_{t\phi})^2 - g'_{tt} g'_{\phi\phi},$$
$$\Phi_o \equiv g'_{t\phi} \Phi_{(+)} - g_{t\phi} (g_{\phi\phi} g_{tt})', \qquad \Phi_\star \equiv g^2_{t\phi} g'_{tt} + g^2_{tt} g'_{\phi\phi} - g_{tt} (g^2_{t\phi})', \tag{12}$$

for $\theta = \pi/2$, where the primes represent the derivative with respect to r. The Keplerian profile intersection with the torus profile determines centers and cusps of the tori. In the standard Kerr spacetime it takes the well-known form

$$\ell_K(r, a) = \ell^{\mp} \equiv \frac{a^3 \mp r^{3/2}\Delta - a(4M - 3r)r}{a^2 - (r - 2M)^2 r}. \tag{13}$$

III. DARK MATTER MODELS

We analyze accretion tori orbiting spinning BHs with spacetimes influenced by different DM models. The metrics reduce, for some limiting values of the DM parameters, to the Kerr BH geometry. Thus, using Eq. (10) we consider the BH DM metric components $\{g_{tt}, g_{t\phi}, g_{\phi\phi}\}$ in BL coordinates, and we refer the reader to the literature for details on the metric tensor and the geometry properties. We investigate the equatorial circular geodesic structures for the fluid effective potential, the effective potential function, and the torus structure for corotating and counterrotating tori in three DM models: In Sec. III A we address the PFDM model of [4]. Cold and scalar field DM models of [8,9] are discussed in Sec. III B.

A. Perfect-fluid dark matter

A rotating BH solution in PFDM was discussed in [4], with

$$g_{tt} = -\left[1 - \frac{2Mr - f_D(r)}{\Sigma}\right], \qquad g_{t\phi} = -\frac{\sigma a [2Mr - f_D(r)]}{\Sigma},$$
$$g_{\phi\phi} = \sigma \left[\frac{a^2 \sigma [2Mr - f_D(r)]}{\Sigma} + (a^2 + r^2)\right], \tag{14}$$

$$g_{rr} \equiv \frac{\Sigma}{\Delta_D}, \qquad g_{\theta\theta} = \Sigma,$$
$$\text{where } \Delta_D \equiv \Delta + f_D(r) \quad \text{and} \quad f_D(r) \equiv kr \log \frac{r}{|k|}. \tag{15}$$

See also [5–7], where k is the parameter describing the intensity of the PFDM, set in the ranges $k \in]-7.18M, 2M[$. For $k = 0$ the line element reduces

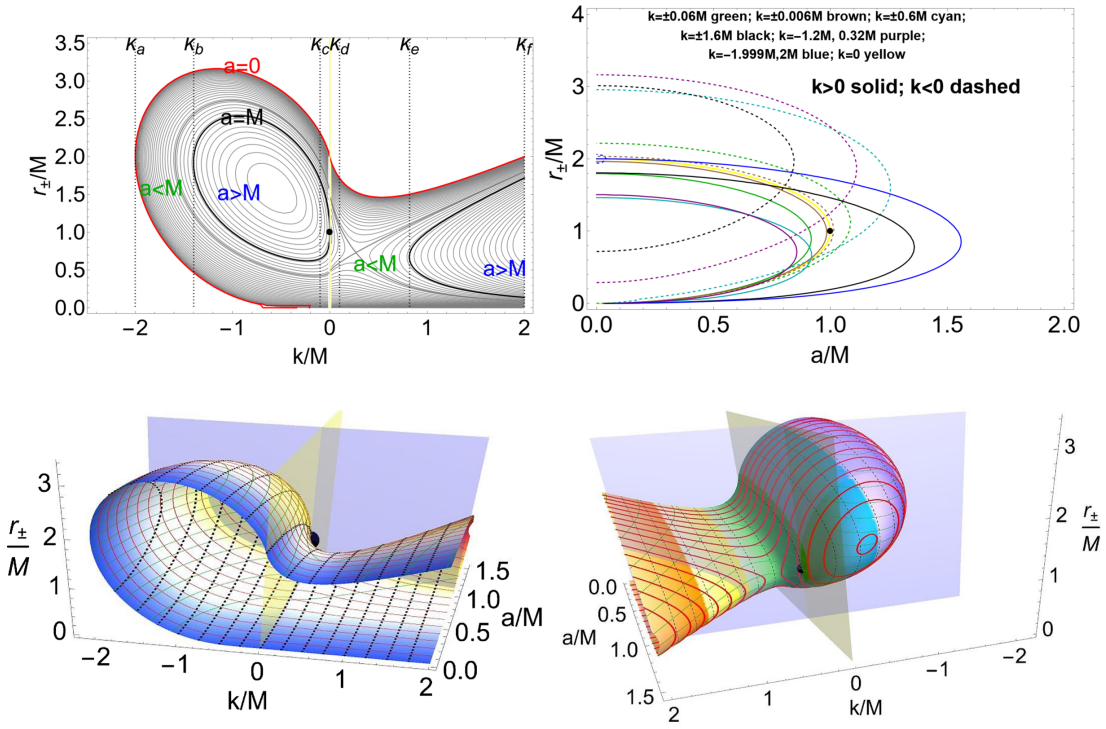

FIG. 2. Horizons and ergosurfaces of the BHs in the PFDM of Eq. (14). Different values of the $k \in]-7.18M, 2M[$ parameter describing the PFDM intensity are considered. (For $k = 0$ the line element describes the Schwarzschild and Kerr geometries in absence of DM.) Upper left panel: horizons $r_\pm$ as functions of the k parameter for different values of the spin $a \geq 0$. Curves at $a \lessgtr M$ are shown. The red curves are the horizons of the static case [$a = 0$) [and the ergosurfaces $r_e^\pm$ Eqs. (16) on the equatorial plane for $a > 0$]. The values $\mathbf{k_6}$ of Eq. (17) are signed as dotted vertical lines. A yellow vertical line labels the Schwarzschild and Kerr geometries in the absence of DM. Upper right panel: horizons $r_\pm/M$ as functions of the spin a/M for different values of $k > 0$ (solid curves) and $k < 0$ (dashed curves). The displayed values are $k = \pm 0.06M$ (green curve), $k = \pm 0.006M$ (brown curve), $k = \pm 0.6M$ (cyan curve), $k = \pm 1.6M$ (black curve), $k = -1.2M, 0.32M$ (purple curve), and $k = -1.999M, 2M$ (blue curve). Curve $k = 0$ (yellow) represents the Schwarzschild and Kerr geometries in the absence of DM. Bottom right and bottom left panels: different views of horizons $r_\pm$ as functions of k/M and a/M. The mesh functions are curves with constants r/M (solid green curve), k/M (dotted gray curve), and a/M (solid red curve). The yellow vertical plane labels the case of $k = 0$. Function contour colors are according to the a/M values (left panel) and k/M values (right panel). We have marked with a black spot the extreme Kerr BH horizon $(a = M, r = M)$ on all panels. To better highlight this point, plane $a = M$ (blue) is included in the bottom panels (the crossing of the $a = M$ and $k = 0$ planes occurs at the point $a = M, k = 0, r = M$).

to the Kerr metric.[16] The metric singularities $r_\pm$ defining the DM deformations on the Kerr horizons can be found by solving the equation $a = a_\pm \equiv \sqrt{r(2M - r) - f_D(r)}$, or from the equation $k = k_\pm \equiv \Delta/[rW(\Delta/r^2)]$, where W is the Lambert function, such that $W(z)$ gives the principal solution for w in $z = we^w$.

The deformed ergosurfaces $r_e^\pm$ can be found for $\sigma \neq 1$ as a solution of the equation $a = a_e^\pm \equiv a_\pm/\sqrt{1-\sigma}$, while on the equatorial plane ($\sigma = 1$)

$$r_e^\pm = \begin{cases} kW\left[\frac{e^{2M/k}}{\mathrm{sgn}(k)}\right] < 2, & \text{for } k \lessgtr 0, \\ kW[-1, -e^{2M/k}] > 2, & \text{for } k < 0, \\ 2, & \text{for } k = 0 \end{cases} \tag{16}$$

[16]The constraints of k/M positive were obtained by fitting the rotation curves in spiral galaxies, with values 10^{-6}–10^{-7} [4].

(see the red curve in Fig. 2, bottom left panel) where the Lambert function $W(s, z)$ gives the sth solution for w in $z = we^w$ and $\mathrm{sgn}(k)$ gives the sign of k. Therefore, it is -1, 0, 1 for k negative, zero, or positive.

The PFDM horizons are independent of σ (as in the Kerr case). The PFDM ergosurfaces are independent of spin in the equatorial plane (as in the Kerr cases). The horizons $r_\pm$ [and the ergosurfaces $r_e^\pm$ on the equatorial plane of Eq. (16)] are shown in Fig. 2.

The red curve in Fig. 2, which represents the BH horizon for $a = 0$ [and the ergosurfaces in Eq. (16) on the equatorial plane for $a \neq 0$], bounds the collections of horizons at different $a = \text{constant}$ in the plane $(r/M, a/M)$. The PFDM metric describes solutions with 0, 1, and 2 horizons. For BH solutions, horizons can be shifted outwardly or inwardly with respect to the Kerr BH spacetime depending on the value of k. There are also spacetime solutions with horizons for $a > M$.

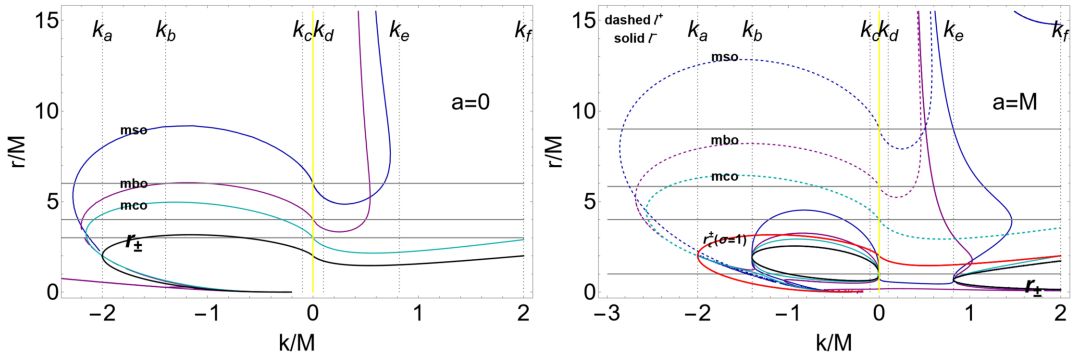

FIG. 3. Equatorial circular geodesic structures of the Kerr attractor in the PFDM of Eq. (14). Different values of the $k \in]-7.18M, 2M[$ describing the PFDM intensity are considered, where for $k = 0$ (vertical yellow line) the line element describes the Schwarzschild (for $a = 0$) and extreme Kerr BH geometry (for $a = M$). Values $\mathbf{k_6}$ of Eq. (17) are designated with dotted vertical lines. Left panel: $a = 0$. Right panel: $a = M$. Radii $r_\pm$ are the horizons, $r_\epsilon^\pm$ are the ergosurfaces on the equatorial plane (coincident with the horizons of the static case). *mso* is for marginally stable orbit, *mbo* is for the marginally bounded orbit, and mco is for marginally circular orbit for corotating fluids ($\ell = \ell^-$, solid curves) and counterrotating fluids ($\ell = \ell^+$, dashed curves). The horizontal gray lines show the radii of the geodesic structure for the Kerr and Schwarzschild BH geometry in the absence of dark matter ($k = 0$) for $a = 0$ and $a = M$, respectively. See also Fig. 1.

Accordingly, we select the PFDM metric parameter in the following six cases:

$$\mathbf{k_6} \equiv \{k_a = -2M, k_b \approx -1.399M, k_c = -0.1M, k_d = 0.1M, k_e \approx 0.82M, k_f \equiv 2M\}. \quad (17)$$

Cases (k_a, k_f) have as horizon $r = 2M$ for $a = 0$ (the static case); therefore, in this sense, these solutions can be compared to the Schwarzschild case. Similarly, for $k = k_b$, the geometry with $a = M$ has one horizon at $r = 2M$. There is one horizon[17] when $k = k_e$ and $a = M$.

In Fig. 4 we show also the fluid specific angular momentum distribution for the $\mathbf{k_6}$ parameters for the cases $a = 0$ and $a = M$ compared to the distribution on the geometry in the absence of DM (see also Fig. 1), the associated K parameter, and the Keplerian (test particle) angular momentum $\mathcal{L}^\pm \equiv \ell^\pm K^\pm$, respectively, which we have defined as related to the thick torus counterparts from the definition of $K(r) \equiv V_{\rm eff}(\ell(r))$, showing the influence of the DM on the limiting thin Keplerian (geodesic) disk. The thin Keplerian disk is constrained by the geodesic structure of the gravitational background.

In general, the geodesic structure is qualitatively similar for any spin (Fig. 3). We focus on the two limiting cases $a = 0$ and $a = M$, whose equatorial circular geodesic structures for the orbiting configurations are represented in Fig. 3. In this model DM couples with the BH rotation, entangled with the frame dragging, as evidenced in the deformed rotational law $\ell^\pm$ of the orbiting matter. According to the DM parameter k and spin a, relation (11), i.e., $r^\pm_{mso} > r^\pm_{mbo} > r^\pm_{mco}$ for the $\ell = \ell^\pm$ cases, holds, as in the nondeformed BH case. According to the discussion in Sec. II B 2 of the Kerr background, this relation, for a small magnitude of k, is reflected in the relative location of the maximum-minimum points of pressure of the orbiting disks. For values of k where this relation is not verified, for example, for $k > 0$ in Fig. 3, the orbiting toroidal structures show large qualitative divergences with respect to the accretion torus formation and dynamics in the Kerr BH spacetime.

The static attractor ($a = 0$).—The geodesic structure is represented in Fig. 3 (left panel) in comparison to the Schwarzschild case. We note that for $k > 0$ the situation changes qualitatively with respect to the case in the absence of DM. Figure 4 shows the fluid specific angular momentum $\ell^\pm$, the torus energy parameter $K^\pm$, and the (test particle) Keplerian angular momentum $\mathcal{L}^\pm$ as functions of r/M for different PFDM parameters of Eq. (14) compared to the case of $k = 0$ describing the Schwarzschild geometry. Notably, for (k_f, k_e), $K(r) > 1$. From the $(\ell^\pm, K^\pm)$ analysis it is noted how, for some values of k, curves are lower with respect to the corresponding curves in the absence of DM; Fig. 3. From the analysis of the curves $L^\pm$, we can note how in some cases the test particle angular momentum is qualitatively different from the corresponding value in the Schwarzschild case. Torus and effective potentials in this case, which are represented in Fig. 5, are constrained by the geodesic structure of Fig. 3.

The spinning attractor ($a > 0$).—The geodesic structure for the spinning attractor geometry in PFDM is in Fig. 3, right panel. The fluid specific angular momentum $\ell^\pm$, energy parameter $K^\pm$, and (test particle) Keplerian angular momentum $\mathcal{L}^\pm$, shown in Fig. 4 as functions

[17]From Fig. 3 we note that there is one horizon at $r \approx 1.583M$ for the special parameters $(a \gtrapprox 1.25776M, k \approx -0.595M)$ and at $r \approx 0.73M$ for $(a \approx 0.855M, k \approx 0.27M)$.

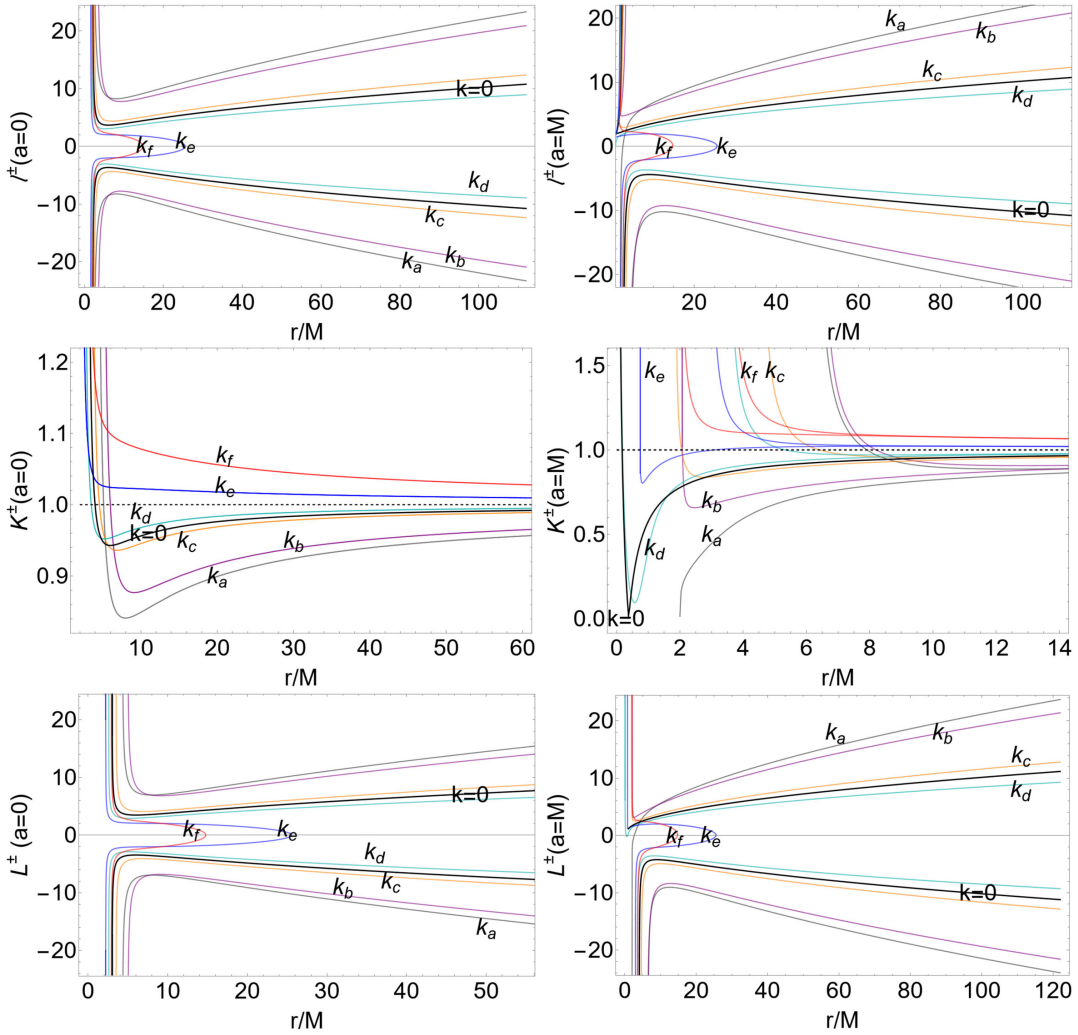

FIG. 4. Fluid specific angular momentum $\ell^{\pm}$, energy parameter $K^{\pm}$, and (test particle) Keplerian angular momentum $\mathcal{L}^{\pm}$ as functions of r/M for corotating and counterrotating fluids, with different PFDM parameters of Eq. (14) indicated in the panels. Different values of the $k \in]-7.18M, 2M[$ parameter describing the PFDM intensity are considered. Columns are $a = 0$ (left) and $a = M$ (right), and rows are $\ell^{\pm}$ (top), $K^{\pm}$ (middle), and $\mathcal{L}^{\pm}$ (bottom). (For $k = 0$ the line element describes the Schwarzschild or the Kerr geometry.) The $\mathbf{k_6}$ values are in Eq. (17).

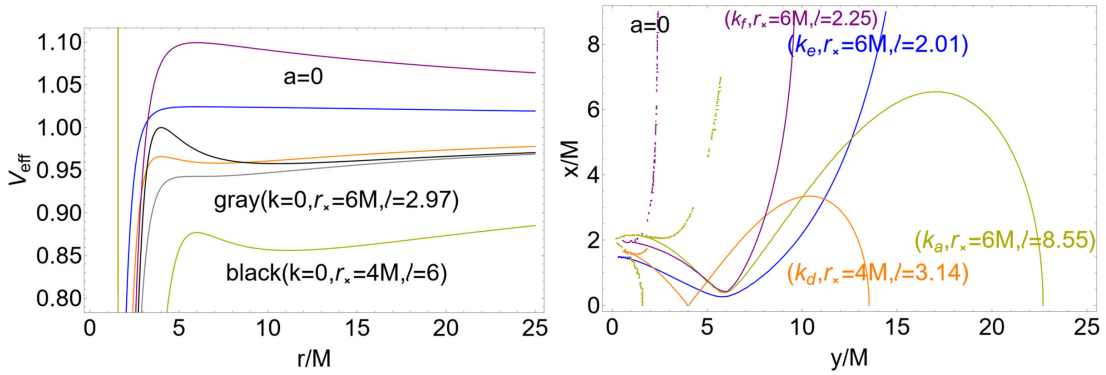

FIG. 5. Case $a = 0$. Torus orbiting BHs in the PFDM of Eq. (14). Left panel: associated torus effective potentials. The $\mathbf{k_6}$ values of Eq. (17) are considered. (For $k = 0$ the line element describes the Schwarzschild geometry.) Right panel: tori for selected values of the k/M parameter, cusp location $r_\times$, and fluid specific angular momentum ℓ signed on the curves. $r = \sqrt{x^2 + y^2}$ and $\sigma = y^2/(x^2 + y^2)$, where $\sigma \equiv \sin^2\theta$.

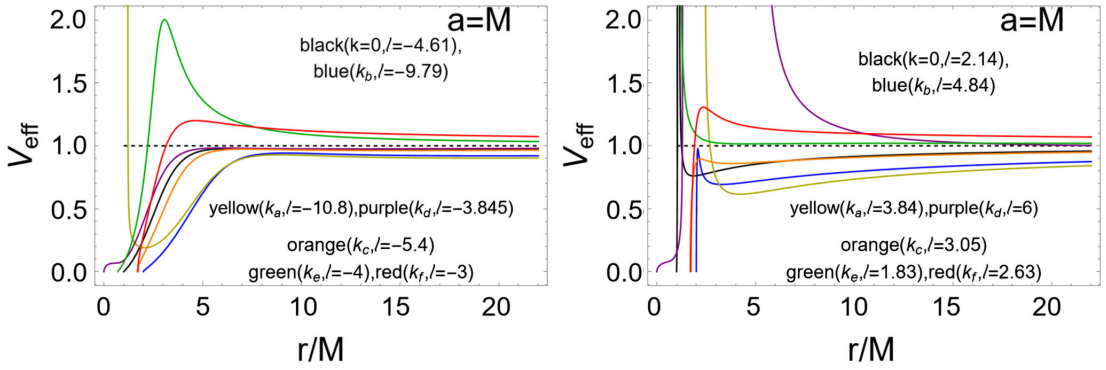

FIG. 6. Case of $a = M$. Effective potentials for torus orbiting BHs in the PFDM of Eq. (14) for different values of the parameter $k \in]-7.18M, 2M[$ that describe the PFDM intensity and fluid angular momentum ℓ are signed on the curves. The $\mathbf{k_6}$ values of Eq. (17) are considered here. (For $k = 0$ the line element describes the extreme Kerr BH geometry.) Left (right) panel: effective potentials for counterrotating (corotating) fluids. $r = \sqrt{x^2 + y^2}$ and $\sigma = y^2/(x^2 + y^2)$, where $\sigma \equiv \sin^2\theta$. There are black curves for $(k = 0, \ell = -4.61, \ell = 2.14)$, blue curves for $(k_b, \ell = -9.79, \ell = 4.84)$, yellow curves for $(k_a, \ell = -10.8, \ell = 3.84)$, purple curves for $(k_d, \ell = -3.845, \ell = 6)$, orange curves for $(k_c, \ell = -5.4, \ell = 3.05)$, green curves for $(k_e, \ell = -4, \ell = 1.83)$, and red curves for $(k_f, \ell = -3, \ell = 2.63)$.

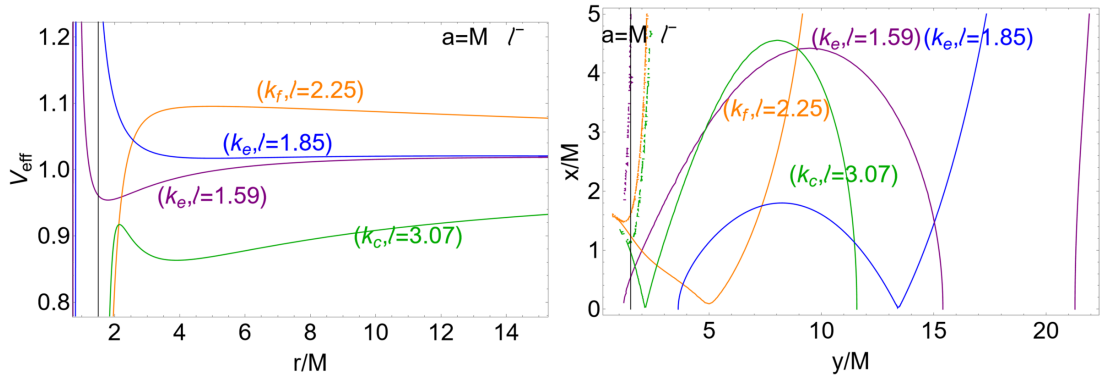

FIG. 7. Case of $a = M$. Effective potentials and torus orbiting BHs in the PFDM of Eq. (14) for different values of the parameter $k \in]-7.18M, 2M[$ that describe the PFDM intensity and fluid specific angular momentum ℓ signed on the curves. Corotating $\ell^- = \ell > 0$ cases are represented. The $\mathbf{k_6}$ values of Eq. (17) are considered here. For $k = 0$ the line element describes the extreme Kerr BH geometry. $r = \sqrt{x^2 + y^2}$ and $\sigma = y^2/(x^2 + y^2)$, where $\sigma \equiv \sin^2\theta$.

of r/M for the corotating and counterrotating fluids and PFDM parameters of Eq. (14), are compared to the case $k = 0$ describing the Kerr geometry in the absence of DM. Torus effective potentials for the counterrotating (corotating) fluids are in Fig. 6. Tori are in Figs. 7 and 8.

As is clear from Fig. 3 the geodesic structure in the DM geometry with $a = 0$ is similar to the counterrotating geodesic structure in the axially symmetric spacetime ($a \neq 0$). The corotating case (for $a = M$), $\ell = \ell^-$, especially for $k > 0$, is remarkably different from the geodesic structure in the geometries with $a = 0$, and it is further complicated by the presence of the ergoregion deformed by the PFDM with, however, quantitative discrepancies with respect to the Kerr spacetime for a large part of the DM parameter values $k < 0$. For larger $k > 0$ there are also NS solutions (for $a \in]0, M]$ as well) and, for even larger values of $k > 0$, there are BH solutions (for $a > M$ as well). In general, DM influence also manifests with the existence of extremely large cusped tori located considerably far from the central singularity, as is clear when one compares the geodesic structures in Fig. 1 and 3. In some cases, as is clear from Fig. 7, there are double configurations at equal ℓ (the purple and blue curves in Fig. 7 and the green curve in Fig. 8), with considerable larger tori with respect to the case in the absence of dark matter. Furthermore, we note the presence of outer cusps (the blue curve in Fig. 7), or possibly the emergence of double cusps, also in the presence of BH solutions, where the corotating marginally stable orbit shows some remarkable peculiarities at $k \geq k_e$ for $a = M$ and $k \in [k_d, k_e]$ for $a = 0$.

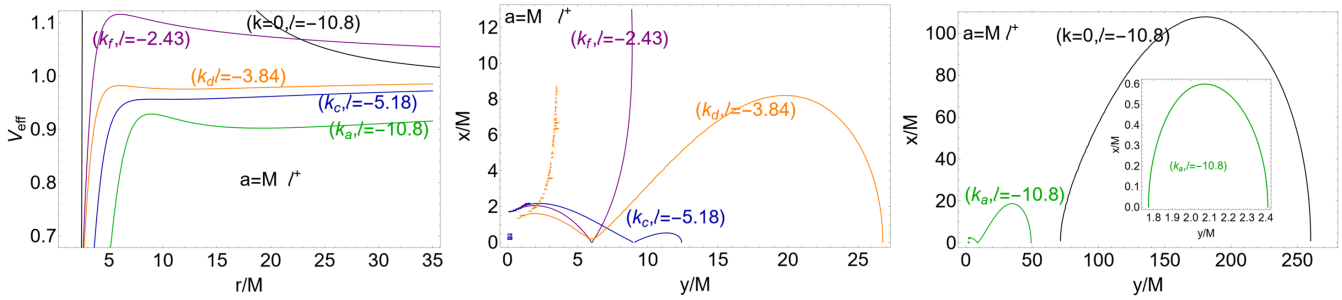

FIG. 8. Case of $a = M$. Effective potentials and torus orbiting BHs in the PFDM of Eq. (14) for different values of the parameter $k \in]-7.18M, 2M[$ describing the PFDM intensity and fluid specific angular momentum ℓ signed on the curves. Counterrotating $\ell^+ = \ell < 0$ cases are represented. The $\mathbf{k_6}$ values of Eq. (17) are considered. For $k = 0$ the line element describes the extreme Kerr BH geometry. The inset in the right panel is an enlargement of the inner green torus. $r = \sqrt{x^2 + y^2}$ and $\sigma = y^2/(x^2 + y^2)$, where $\sigma \equiv \sin^2\theta$.

The interdisk cusp[18] (see also Fig. 7) can evolve following the change in one or two of the torus parameters (ℓ, K) in an inner cusp followed by an inner configuration (such as the green curve in Fig. 8) or two separate configurations (such as the purple curve in Fig. 7). For $k = k_e$, in the case $a = M$, there are no horizons. Consequently, the geometry, although not overspinning, can be considered a naked singularity, and the green curve in Fig. 8 can be seen as a typical double configuration characterizing certain NS geometries. Also, the presence of excretion cusps could be a DM indicator. Notably, these features are usually read as tracers for the possible NSs observations, emerging as consequences of the repulsive gravity effects characterizing NSs solutions, and in this sense the Kerr BH immersed in PFDM could be a "mimicker" of superspinar solutions.

B. Cold and scalar field dark matter

In this section we consider a spinning BH in SFDM (addressed in Sec. III B 1) and in CDM (considered in Sec. III B 2); see, for example, [8,9].

1. Scalar field dark matter

There is

$$g_{tt} = -\left[1 - \frac{2Mr + r^2(1-\xi_{\rm SFDM})}{\Sigma}\right],$$
$$g_{t\phi} = -\frac{a\sigma[2Mr + r^2(1-\xi_{\rm SFDM})]}{\Sigma},$$
$$g_{\phi\phi} \equiv \frac{\sigma[(a^2+r^2)^2 - a^2\sigma\Delta_{\rm SFDM}]}{\Sigma}\, g_{rr} \equiv \frac{\Sigma}{\Delta_{\rm SFDM}}, \qquad g_{\theta\theta} = \Sigma, \tag{18}$$

where

$$\Delta_{\rm SFDM} \equiv a^2 - 2Mr + r^2\xi_{\rm SFDM} \quad \text{and}$$
$$\xi_{\rm SFDM} \equiv \exp\left[-\frac{8\rho_c R^2 \sin(\frac{\pi r}{R})}{\frac{\pi(\pi r)}{R}}\right]. \tag{19}$$

The metric components satisfy the asymptotic flatness condition, and the fluid potential is well defined at infinity $(r \to +\infty)$, where $V_{\rm eff} = 1$. We introduce the quantity $k{:}\rho_c = k/R^3$. Here ρ_c is the central density and R is the radius at which the pressure and density are zero[19] (where for $\rho_c = 0$ the metric reduces to the Kerr solution). The Kerr limit occurs for $k \to 0$ *or* $R \to +\infty$. The zeros of $\Delta_{\rm SFDM}$ distinguish the metric singularities $r_\pm$ (SFDM deformed horizons), while the zeros of g_{tt} define a deformation of the Kerr ergosurfaces $r_e^\pm$, which can be found by solving the equations $a = a_\pm$ and $a = a_e^\pm$, respectively,[20] where

$$a_\pm \equiv \sqrt{r(2M - r\xi_{\rm SFDM}^{-1})}, \qquad a_e^\pm \equiv \frac{a_\pm}{\sqrt{1-\sigma}}, \quad \text{with}$$
$$\xi_{\rm SFDM} \equiv e^{\frac{8k\sin(\frac{\pi r}{R})}{\pi^2 r}}. \tag{20}$$

In accordance with the study of the BH horizons in Fig. 9, we explore the following two cases:

$$\mathcal{F}_p \equiv \{k_p \to 1000M, R_p \to 1200M\},$$
$$\mathcal{F}_g \equiv \{k_g \to 20000M, R_g \to 120000M\} \tag{21}$$

(see Fig. 9).

[18]Like the outer cusps, the interdisk cusp is a torus cusp located between two configurations having the same (ℓ, K) parameters, which eventually could be interpreted as an excretion cusp characterizing some cosmological models; see, for example, the double separated configurations (purple curves) or the blue curve in Fig. 7.

[19]In the SFDM static solution, the Klein-Gordon equation and a quadratic potential for the scalar field have been considered [8,9].

[20]The accretion tori considered here are geometrically thick and characterized by a pronounced verticality. The torus surfaces can therefore approach the outer ergosurface out of the equatorial plane (i.e., $\sigma < 1$). The ergosurface location (on planes $\sigma \neq 1$) is an important factor regulating the Lense-Thirring effect on the disks and on the jet flows coming from the disks [77].

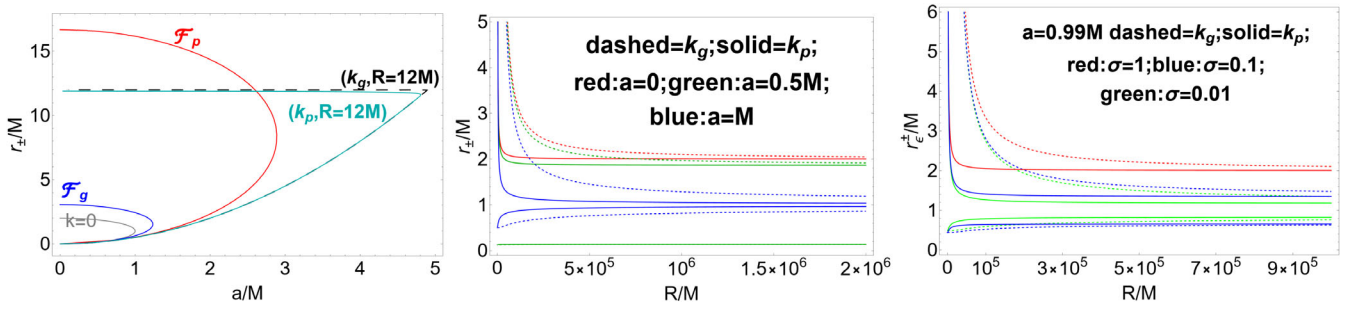

FIG. 9. Horizons and ergosurfaces of BHs geometries in the SFDM of Eq. (19). Parameters $\mathcal{F}_p$ and $\mathcal{F}_g$ are as defined in Eqs. (21). The case of $k = 0$ corresponds to Kerr or Schwarzschild geometries. Left panel: BH horizons $r_\pm$ as functions of a/M for different DM parameters (k, R). The gray curve is the Kerr BH horizon. Center panel: the horizon radii $r_\pm$ as functions of the DM parameter R for different k and spin a, red curve, for $a = 0$ are the static limiting case and $a = M$ is the blue curve, while $a = 0.5M$ is the green curve. The dashed curves correspond to k_g and solid curves to k_p. Right panel: the ergosurfaces as functions of R/M for different k/M for spin $a = 0.99M$ and different planes $\sigma \equiv \sin^2\theta$, $\sigma = 1$ (red curve) are the equatorial plane, the green curve is $\sigma = 0.01$, the blue curve is $\sigma = 0.1$, the dashed curves correspond to k_g and the solid curves to k_p are as defined in Eqs. (21).

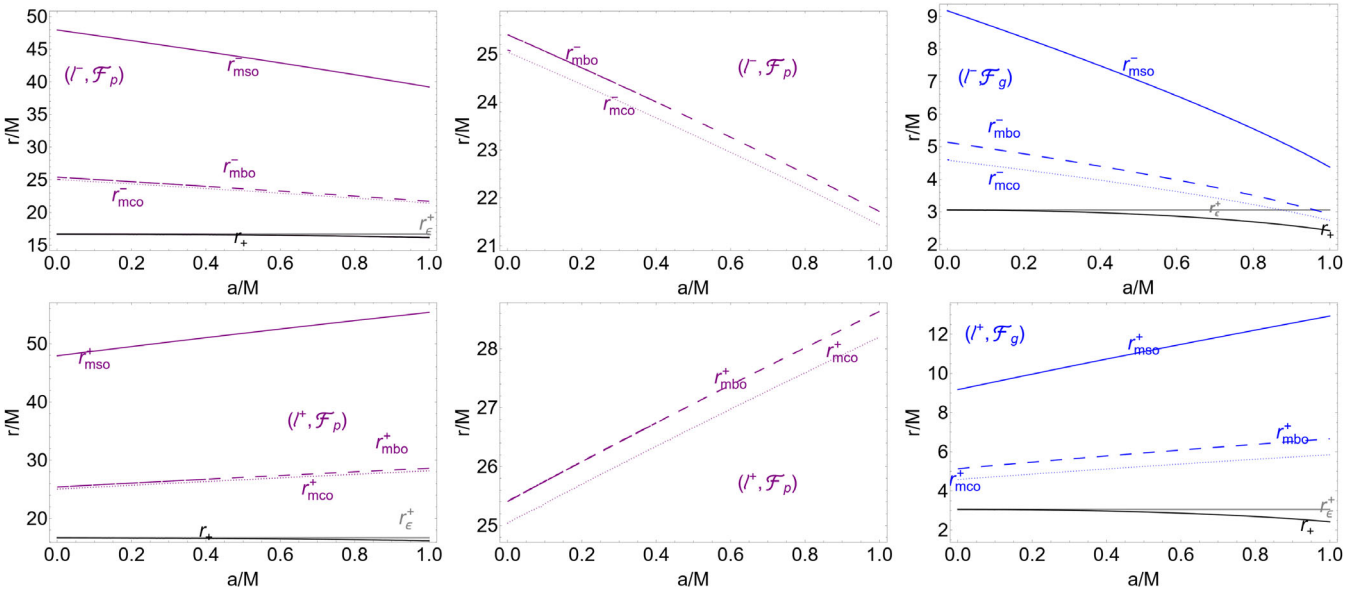

FIG. 10. Geodesic equatorial structure of SFDM geometry of Eq. (19). Upper (lower) panels show the situation for corotating (counterrotating) fluids with ℓ^- (ℓ^+) for parameters $\mathcal{F}_p$ (purple curves) and $\mathcal{F}_g$ (blue curves), as defined in Eqs. (21). Radius r_+ (black curve) is the outer horizon, r^+_ϵ (gray curve) is the outer ergosurface on the equatorial plane, *mso* (solid purple and blue curves) is for a marginally stable orbit, *mbo* (dashed curves) is for the marginally bounded orbits, and mco (dotted curves) is for the marginally circular orbits. The corresponding Kerr geodesic structure is in Fig. 1. Center panels: enlargements of the left panels.

However, as is clear from Fig. 9, BH horizons also exist for $a > M$.

The geometry circular geodesic structure is shown in Fig. 10 for the parameters $\mathcal{F}_g$ and $\mathcal{F}_p$ and emphasizes the differences between the cases (k_p, R_p) and (k_g, R_g) and the Kerr geometry circular structure of Fig. 1. The orbital range in which the protojets cusps are located, bounded by the radii $r^\pm_{mbo}$ and $r^\pm_{mco}$, for fluid specific angular momentum $\ell = \ell^\pm$ is very narrow, and in general the geodesic structure is shifted considerably outward with respect to the Kerr geometry geodesic radii. Therefore, the range for the location of the accreting disk's inner edges is considerably larger than the protojet cusp range, possibly constituting a constraint on the formation of protojets and tori with large angular momentum magnitudes. We also note that in the corotating case, for $a \in]0, M]$ and for a $\mathcal{F}_p$ that differs from the Kerr case in the absence of DM, radii are located out of the ergoregion (and partially for $\mathcal{F}_g$). This could imply a significant difference in the Lense-Thirring effects in the presence of DM. [There may, however, be overspinning BHs (with $a > M$) where these effects could be present.] Unlike the PFDM case, qualitatively the geodesic structure is not differentiated with respect to the case in the absence of SFDM for corotating or

counterrotating fluids, and for static attractors ($a = 0$) and spinning attractors ($a \in]0, M]$) with SFDM.

We analyze below the case of the static attractor, i.e., $a = 0$, having the Schwarzschild metric as a limit in the vacuum, we then studied the influence of the central attractor spin combined with dark matter effects by considering the case $a = M$, which corresponds to the DM deformation of the vacuum solution (i.e., in the absence of DM) of the extreme Kerr BH, and the case of the slowly spinning attractor having $a = 0.1M$. Let us provide the analysis in more detail.

The static attractor ($a = 0$).—In Fig. 11 the fluid specific angular momentum $\ell^{\pm}$, torus energy parameter $K^{\pm}$, and (test particle) Keplerian angular momentum $\mathcal{L}^{\pm}$ are shown as functions of r/M for corotating and counterrotating fluids, at different spins and SFDM parameters, compared to the case $k = 0$ corresponding to the Schwarzschild geometry. Tori and effective potentials are in Fig. 12.

The spinning attractors ($a = M$ and $a = 0.1M$).—We restrict our analysis to $a = M$ and $a = 0.1M$ while studying the cusped tori limiting the closed configurations regulated by the effective potential function. In Fig. 11, there are the fluid specific angular momentum $\ell^{\pm}$, the energy parameter $K^{\pm}$, and the (test particle) Keplerian angular momentum $\mathcal{L}^{\pm}$ as functions of r/M for corotating and counterrotating fluids, different spins, and the SFDM parameters of Eq. (19) with respect to the Kerr vacuum cases. In Fig. 12 are the fluids effective potentials and tori compared to the case of Kerr in the absence of DM. From Fig. 11 we note that within this parameter choice, unlike the case in which DM is absent, the fluid's energy function cannot converge to 1 for large values of r. In Fig. 11 the fluid specific angular momentum distribution, compared to

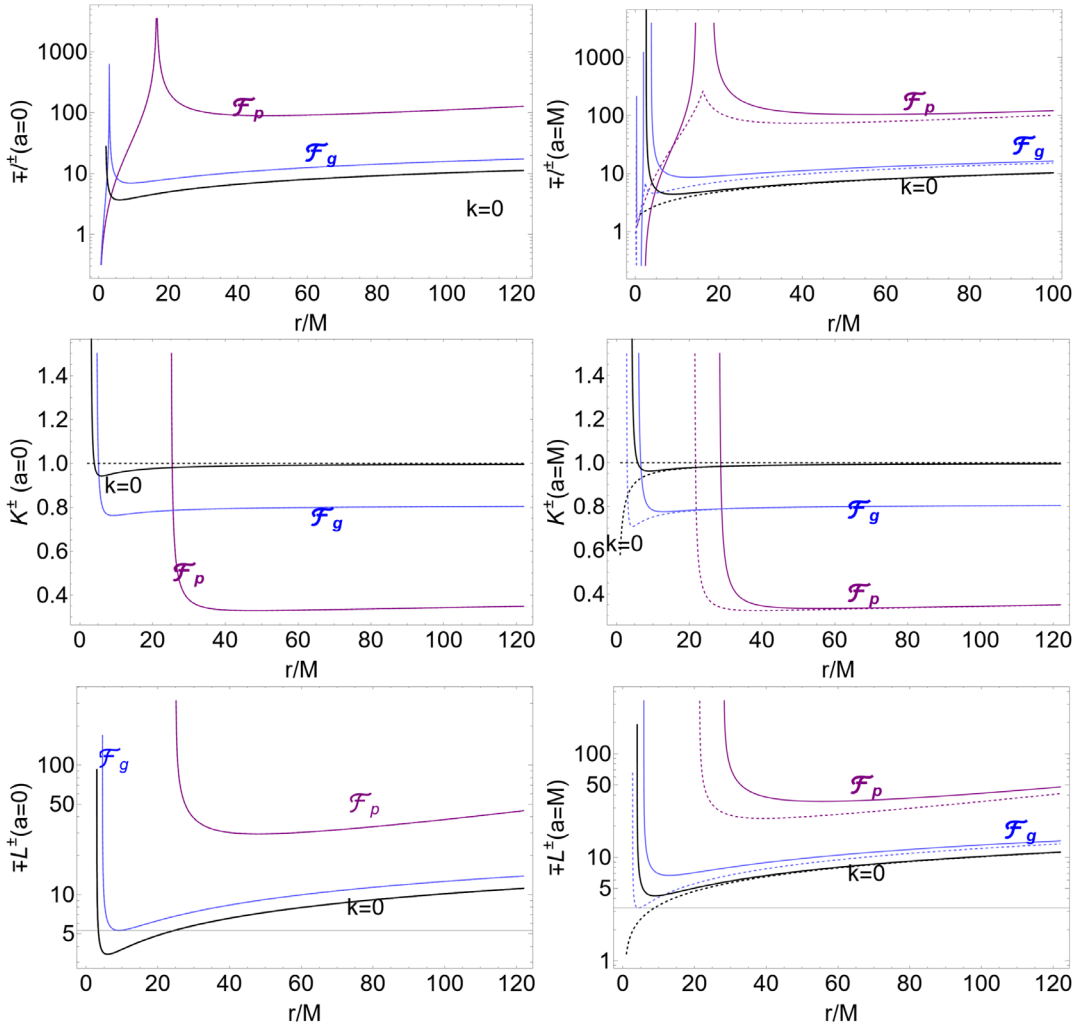

FIG. 11. Fluid specific angular momentum $\ell^{\pm}$, energy parameter $K^{\pm}$, and (test particle) Keplerian angular momentum $\mathcal{L}^{\pm}$ as a function of r/M for corotating $(-)$ and counterrotating $(+)$ fluids and different SFDM parameters $\mathcal{F}_p$ (purple) and $\mathcal{F}_g$ (blue), as defined in Eqs. (21). The value $k = 0$ corresponds to the Schwarzschild ($a = 0$) extreme Kerr BH case ($a = M$). The columns are $a = 0$ (left panels) and $a = M$ (right panels), and rows are for ℓ as function of r (top), K as function of r (middle panels), $\mathcal{L}$ as function of r (bottom panels).

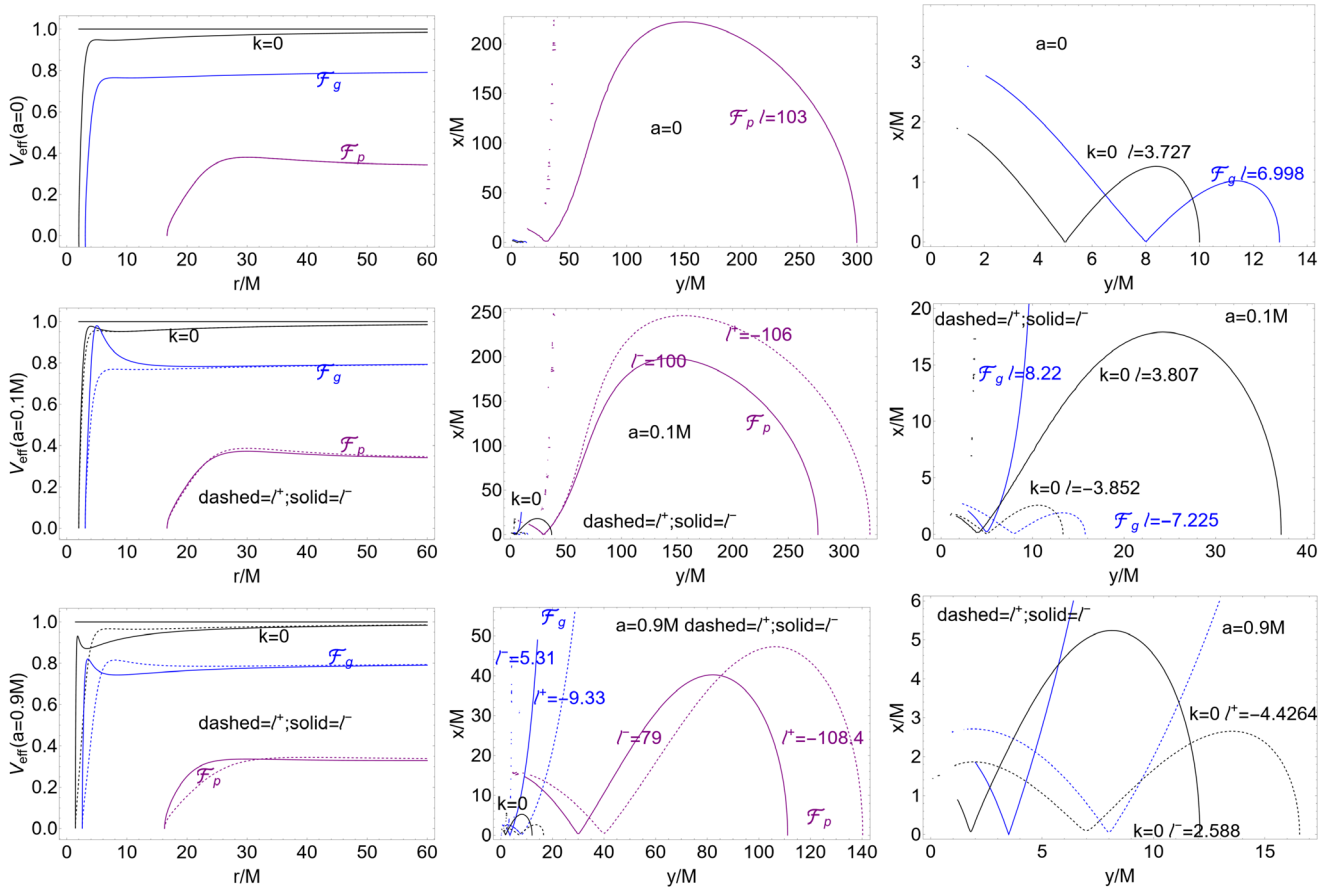

FIG. 12. Fluids effective potentials (left panels) and tori (center and right panels) orbiting in scalar field dark matter (SFDM) geometry of Eq. (19), with parameters $\mathcal{F}_p$ (purple curves) and $\mathcal{F}_g$ (blue curves), as defined in Eqs. (21). The geodesic structure is in Fig. 10. The displayed rows are $a = 0$ (top panels), $a = 0.1M$ (middle panels), and $a = 0.9M$ (bottom panels). Black curves for $k = 0$ are the configurations for the case of Schwarzschild and Kerr spacetimes in the absence of DM. Tori are shown in the corresponding colors relative to the effective potentials. Fluid specific angular momenta ℓ^+ (dashed curves) and ℓ^- (solid curves) are signed close to each tori surface (center and right panels). Right panels: enlargement of the center panels in the region close to the central attractor. (The integration is in the entire orbital range.) $r = \sqrt{x^2 + y^2}$ and $\sigma = y^2/(x^2 + y^2)$, where $\sigma \equiv \sin^2\theta$.

the distribution on the geometry in the absence of DM, the associated K energy parameter and the Keplerian (test particle) angular momentum $\mathcal{L}^\pm \equiv \ell^\pm K^\pm$ are shown. From Fig. 9 it is clear how the horizon curves in the plane $a - M$ are larger and shifted outward with respect to the Kerr BH case, constituting a discriminant for the SFDM model. For some values of the DM parameters, the BH horizons disappear, giving rise to a "DM-induced" NS.

Large torus orbiting SFDM spinning BHs are shown in Fig. 12 as, for example, the purple surface for the case $a = 0$ (from the torus effective potentials we can also note how the torus K parameter for tori orbiting in SFDM are generally considerably lower than the K parameter in absence of DM). This feature of the DM model could also be an indication that such extremely large tori are actually not formed, and similarly the backreaction on the metric is a predominant factor in these configurations, where self-gravity becomes a determinant factor in the torus equilibrium.

2. Cold dark matter

The metric components read

$$g_{tt} = -\left[1 - \frac{2Mr - \xi_{\rm CDM} + r^2}{\Sigma}\right], \qquad g_{t\phi} = -\frac{a\sigma[2Mr - \xi_{\rm CDM} + r^2]}{\Sigma}, \qquad g_{\phi\phi} \equiv \frac{\sigma[(a^2 + r^2)^2 - a^2\sigma\Delta_{\rm CDM}]}{\Sigma};$$
$$g_{rr} \equiv \frac{\Sigma}{\Delta_{\rm CDM}}, \qquad g_{\theta\theta} = \Sigma, \tag{22}$$

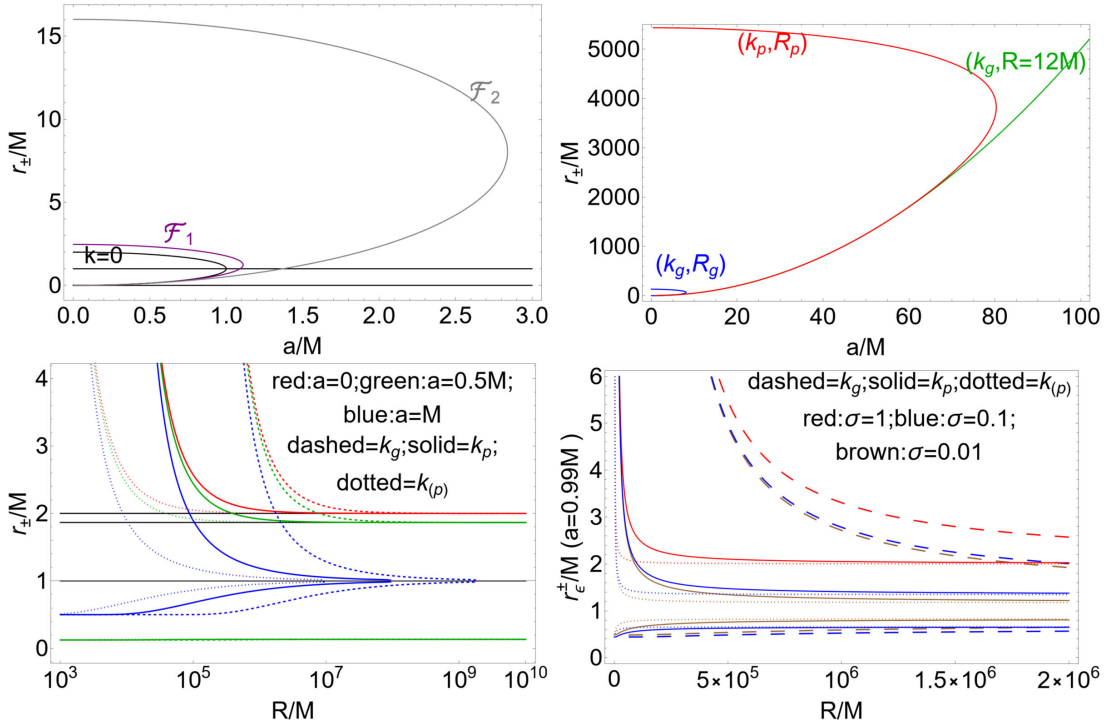

FIG. 13. Horizons $r_\pm$ and ergosufaces $r_\epsilon^\pm$ of the CDM geometry of Eqs. (22). The dark matter parameters $\mathcal{F}_1$, $\mathcal{F}_2$, and $k_{(p)}$ are from Eqs. (26), while the parameters (k_p, k_g, R_g, R_p) are from Eqs. (21). The black curves ($k = 0$) correspond to the Kerr horizons. $\sigma \equiv \sin^2\theta$, where $\sigma = 1$ is the equatorial plane. In the bottom left panel the blue curves are for $a = M$, the red curves are for $a = 0$, the green curves are for $a = 0.5M$, the dotted curves are for $k = k_{(p)}$, the dashed curves are for $k = k_g$, the solid curves are for $k = k_p$, and the black horizontal lines correspond to $k = 0$ for the Kerr spacetimes. Bottom right panel: ergosurfaces $r_\epsilon^\pm$ as a function of the dark matter parameter R/M for spin $a = 0.99M$ and for different planes $\sigma \in [0, 1]$ and dark matter parameter k, where the red curves correspond to $\sigma = 1$, the blue curves correspond to $\sigma = 0.1$, the brown curves correspond to $\sigma = 0.01$, the dashed curves are for $k = k_g$, the solid curves are for $k = k_p$ and the dotted curves are for $k = k_{(p)}$.

where

$$\Delta_{\rm CDM} \equiv a^2 - 2Mr + \xi_{\rm CDM} \quad \text{and} \quad \xi_{\rm CDM} \equiv r^2\left(\frac{r}{R}+1\right)^{-\frac{8\pi\rho_c R^3}{r}}. \tag{23}$$

We adopt the parametrization $\rho_c = k/R^3$, where ρ_c is the density of the Universe at the moment when the DM halo collapsed and R is a characteristic radius. The metric is asymptotically flat, and we find the Kerr limit in $k \to 0$ or $R \to +\infty$. We first consider the metric singularities, identifying the space of the parameters used in the torus analysis. The horizons $r_\pm$ can be written as solutions of the equation $a = a_\pm(CDM)$, $R = R_\pm(CDM)$, or $k = k_\pm(CDM)$, where

$$a_\pm(CDM) \equiv \sqrt{r[2M - r\wp^{-\frac{8\pi k}{r}}]},$$
$$R_\pm(CDM) \equiv r\left[\frac{1}{1-\varsigma^{\frac{r}{8\pi k}}} - 1\right], \qquad k_\pm(CDM) \equiv \frac{r\log\varsigma^{-1}}{8\pi\log\wp},$$
$$\text{with} \quad \wp \equiv \frac{r}{R}+1 \quad \text{and} \quad \varsigma \equiv \frac{2rM - a^2}{r^2}. \tag{24}$$

The metric horizons are defined for

$$a \in]0, M] : r \in]r_\circledast, r_-[; \quad a \in [0, M] : r > r_+;$$
$$a > M : r > r_\circledast, \quad \text{where } r_\circledast \equiv \frac{a^2}{2M}$$

(assuming that $a > 0$, $R > 0$, and $k > 0$).

The ergosurfaces $r_\epsilon^\pm$ can be found for $\sigma \neq 1$ as solutions of the equation $a = a_\epsilon^\pm(CDM) \equiv a_\pm(CDM)/\sqrt{1-\sigma}$ and, on the equatorial plane ($\sigma = 1$), as solutions of $R = R_\epsilon^\pm$ or $k = k_\epsilon^\pm$, where[21]

$$k_\epsilon^\pm \equiv \frac{r\log\frac{r}{2M}}{8\pi\log\wp} \quad \text{and} \quad R_\epsilon^\pm \equiv r\left[\frac{1}{1-(\frac{2M}{r})^{\frac{r}{8\pi k}}} - 1\right] \tag{25}$$

(see Fig. 13). On the equatorial plane, the outer ergosurface, independent of the spin a, corresponds to the metric singularity in the static ($a = 0$) case; see Eq. (24).

[21]As is clear in Fig. 13, these relations also represent some portions of the ergosurfaces, according to conditions on the DM parameters.

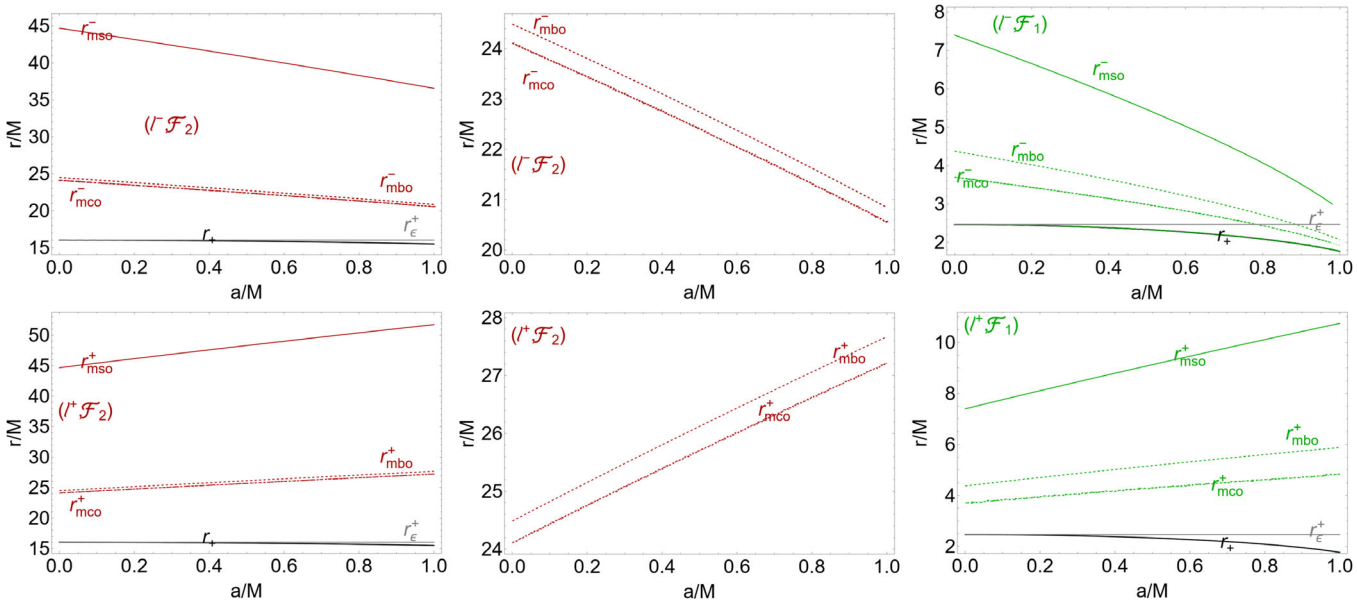

FIG. 14. Geodesic equatorial structure of the CDM geometry of Eqs. (22). The dark matter parameters $\mathcal{F}_1$ (green curves) and $\mathcal{F}_2$ (red curves) are in Eqs. (26). Upper (lower) panels: the structure for fluid specific angular momentum $\ell = \ell^- > 0$ ($\ell^+ < 0$) for corotating (counterrotating) fluids. Center panels: enlargements of the right panels showing the marginally stable orbits (*mso* solid curves), marginally bounded orbits (*mbo* dashed curves), and marginally circular orbits $r^\pm_{mco}$ (dotted curves), where r_+ (black curves) is the outer horizon and r^+_c (gray curves) is the outer ergosurface on the equatorial plane. The corresponding Kerr geodesic structure is in Fig. 1.

We consider the following sets of parameters:

$$\mathcal{F}_1 \equiv \{k \to 1000M, R \to 120000M\},$$
$$\mathcal{F}_2 \equiv \{k \to 100M, R \to 1200M\}, \quad \text{and} \quad k_{(p)} \equiv 100M \tag{26}$$

(Fig. 13). The geodesic structure for this geometry is shown in Fig. 14. As in the SFDM model, the equatorial geodesic structure shows that for the $\mathcal{F}_2$ case the range $[r^\pm_{mco}, r^\pm_{mbo}]$ of the protojet cusp location is remarkably narrow. At $a \in]0, M]$, for corotating fluids, the radii for $\mathcal{F}_1$ ($\mathcal{F}_2$) do not enter (are partially contained in) the outer ergoregion. We have analyzed the static and spinning attractors as follows.

The static attractor ($a = 0$).—The fluid specific angular momentum $\ell^\pm$, the energy parameter $K^\pm$, and the (test particle) Keplerian angular momentum $\mathcal{L}^\pm$ as functions of r/M and the CDM parameters $\mathcal{F}_1$ and $\mathcal{F}_2$ are shown in Fig. 15 compared to the Schwarzschild case. The effective potential and tori are shown in Fig. 16 compared to the Schwarzschild case.

The static attractor ($a = 0$).—The fluid specific angular momentum $\ell^\pm$, the energy parameter $K^\pm$, and the (test particle) Keplerian angular momentum $\mathcal{L}^\pm$ as functions of r/M are represented in Fig. 15 for corotating and counterrotating fluids, different spins, and CDM parameters $\mathcal{F}_1$ in comparison to the extreme Kerr BH case in the absence of DM. The effective potential and tori for the CDM parameters $\mathcal{F}_1$ and $\mathcal{F}_2$ are in Fig. 16 for $a = M$ and $a = 0.7M$ for fluid specific angular momentum $\ell = \ell^- > 0$ ($\ell^+ < 0$) for corotating (counterrotating) fluids compared to the case in the vacuum Kerr geometry. It can be proved that, in all the cases considered, the limit $K \to 1$ for large r holds, where $\mathcal{L}^\pm \equiv \ell^\pm K^\pm$. Large torus orbiting CDM spinning BHs are shown in Fig. 16 as, for example, the blue surface for the case $a = 0$ and the dashed-blue curve for $a = 0.7M$ and $a = M$ (as in the SFDM case, the torus K parameter for tori orbiting in CDM are generally considerably lower than the K parameter in the absence of DM). From Fig. 16 we note, as with SFDM, the presence of larger cusped tori located far from the central spinning attractor, which distinguishes the DM deformed geometry from the Kerr case.

IV. DISCUSSION AND FINAL REMARKS

In the DM models considered here there are NS solutions, solutions with one horizon and two horizons, according to the DM parameters. There are also BH spacetime solutions with horizons at $a > M$ or NSs for $a < M$. The geodesic structure regulating the accretion physics and the torus location around the central spinning attractor can be shifted considerably outward with respect

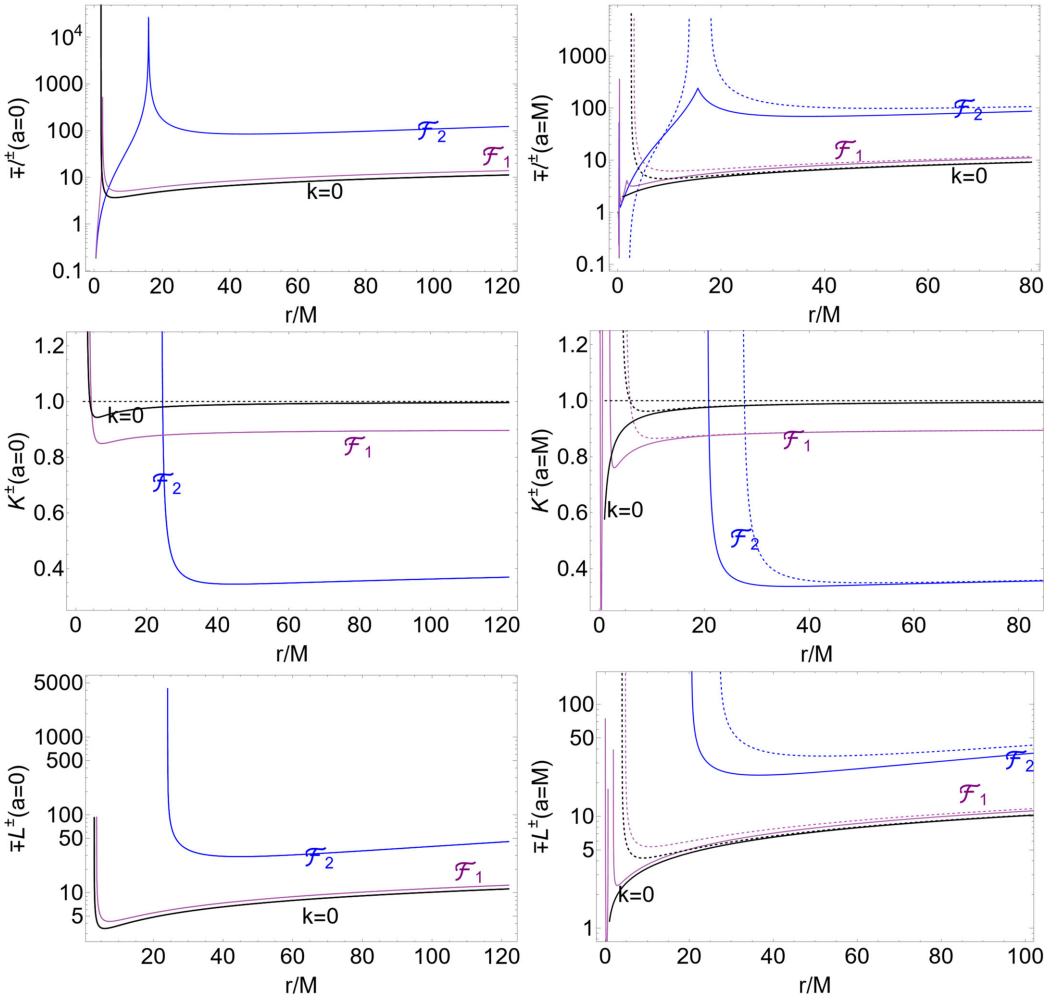

FIG. 15. Fluid specific angular momentum $\ell^{\pm}$ (top row), energy parameter $K^{\pm}$ (middle row), and (test particle) Keplerian angular momentum $\mathcal{L}^{\pm}$ (bottom row) as functions of r/M for corotating and counterrotating fluids and different CDM parameters of Eqs. (22). The dark matter parameters $\mathcal{F}_1$ (purple curves) and $\mathcal{F}_2$ (blue curves) are from Eqs. (26). The columns are $a = 0$ (left) and $a = M$ (right). The Kerr and Schwarzschild cases are the black curves for $k = 0$.

to the Kerr geometry. DM effects mimic Kerr attactors with an altered spin-to-mass ratio a/M. For example, in all the models presented, the DM affects the disk's inner edge, which is a tracer of the a/M ratio in the Kerr geometry. The presence of an excretion cusp, double cusps, or double tori, which are also typical of Kerr NS solutions, could indicate the presence of DM. Consequently, DM affects BH horizon physics by considering DM (models) as NS mimickers or, conversely, DM (models) as BH mimickers for superspinar (cosmological) solutions. DM could also affect the jet emission. The orbital range locating the protojet cusps can also be very small, as discussed in Sec. III B 1 for SFDM and in Sec. III B 2 for CDM. The open cusped solutions (also constraining the jet emission) are very different from their counterparts in the Kerr spacetime in the absence of DM. In general, DM also manifests with the existence of extremely large cusped tori orbiting very far from the central singularity. From Fig. 12 we see the large dimensions of the cusped torus orbiting SFDM spinning BHs. The equilibrium of these tori may be hugely affected by their self-gravity.

In all DM models considered here, however, DM affects the geometric and causality properties, while there is no coupling with ordinary matter (nor is there a hypothetical accretion disk consisting of dark matter in orbit), considering gravity modified by the effects of dark matter; see also [76]. We addressed three models, drawing qualitative and comparative considerations, ruling out some solutions and tracing some common patterns. We have taken as a selection criterion in the space of the metric parameters the observation that there are two expected regimes, where there is a fully modified geometry, qualitatively divergent with respect to the general relativistic onset, as a strongly

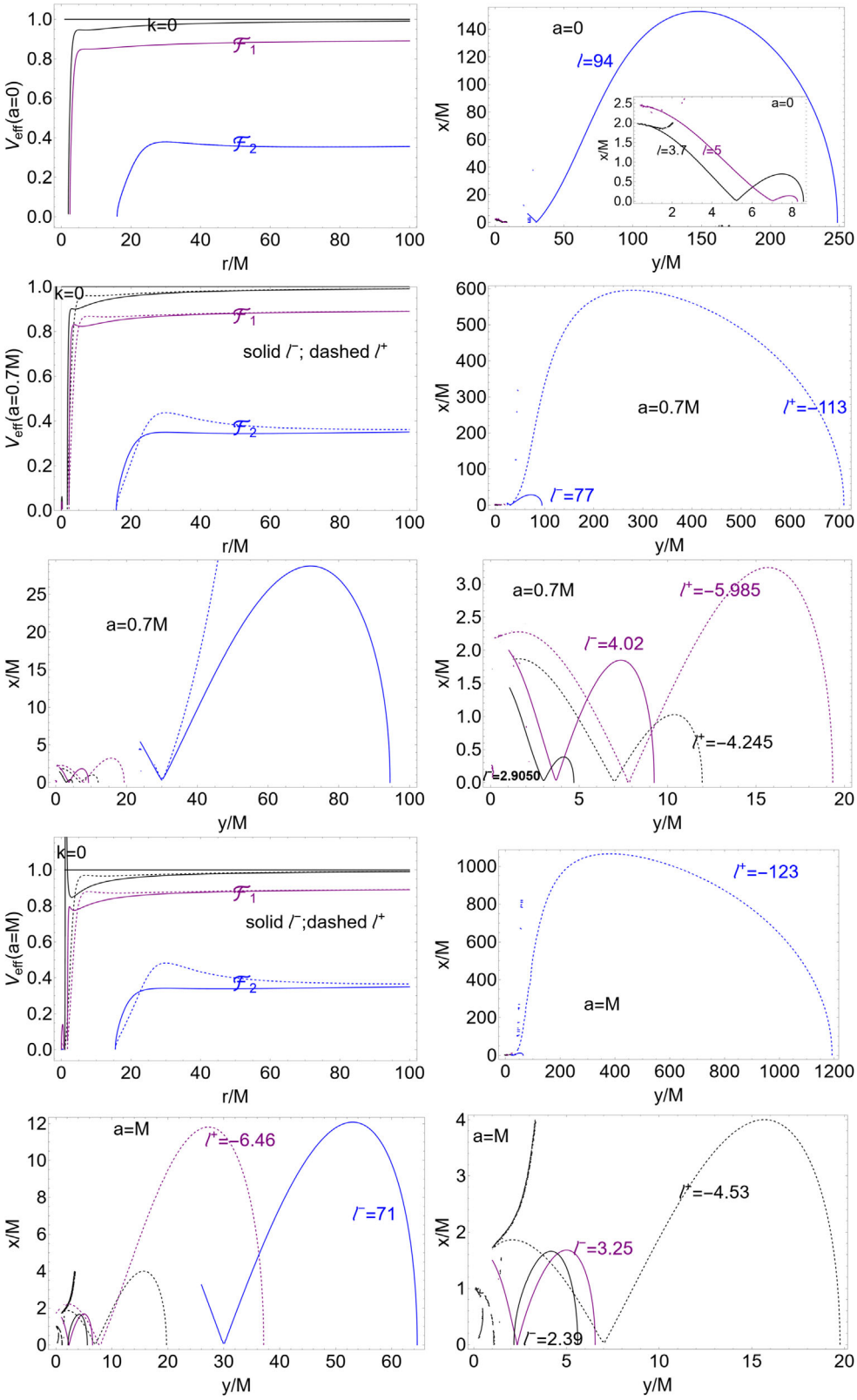

FIG. 16. Effective potential and tori of the CDM geometry. The dark matter parameters $\mathcal{F}_1$ (purple curves) and $\mathcal{F}_2$ (blue curves) are from Eqs. (26). The rows are $a = 0$ (top line), $a = 0.7M$ (top, second, and third lines), $a = M$ (top, fourth, and fifth lines). The black curves for $k = 0$ are the configurations for the cases of Schwarzschild and Kerr spacetimes in the absence of DM. Tori are shown in the corresponding colors association relative to the effective potentials. Fluid specific angular momenta ℓ^+ (dashed curves) and ℓ^- (solid curves) are signed close to each torus surface. Regions close to the central attractor are also shown as enlargements. $r = \sqrt{x^2 + y^2}$ and $\sigma = y^2/(x^2 + y^2)$, where $\sigma \equiv \sin^2\theta$.

different horizon structures than the referenced Kerr solution, and the second scenario consisting of an appreciable quantitative deformation of the orbiting structures, but not a qualitatively significant change of the background geometry defined by the spinning BH. The current methods of measuring and identifying BHs are also based on the physics of accretion. This is related to the accretion disk inner edge, which we prove to be distorted by the DM treated, in the metric models considered here, as a background deformation.

Spherically symmetric black hole solutions in PFDM have been considered to be adapted to the observed asymptotically flat rotation velocity in spiral galaxies and a possible interaction between the DM halo and central BH has been differently theorized. However, it has been supposed that SMBHs could enhance the DM density significantly.[22] The results of our analysis prove accretion to be a good indicator of the divergences induced by the DM presence and the study of the accretion disks in DM models to represent a valid DM model discriminant. The torus dimensions provide an indication of the possible effects of DM for the energetics associated with the physics of accretion around BHs. In the PD models, for example, the thickness of the accretion throat (opening of the cusp for tori with specific fluid angular momentum in **L1** with $K \in]K_\times, 1[$) determines (in the assumptions of vanishing pressure at the inner edge) many characteristics of torus energetics, such as mass accretion rates and cusp luminosity, the rate of the thermal energy carried at the cusp, the mass flow rate through the cusp (i.e., mass loss accretion rate), the fraction of energy produced inside the flow and not radiated through the surface but swallowed by central BH, mass flux, the enthalpy flux (related to the temperature parameter), which also depends on the EOS, as the polytropic index and constant.[23] It has been shown in [71,72] that the maximum of flow thickness and the maximum amount of matter swallowed by the central BH is determined by the attractor spin-mass ratio only, which is defined by the location of the marginally stable circular orbit, and therefore DM influences the torus dimension and the marginally stable orbits in these models can be searched in a variation of the central BH energetics[24] [62,63,72].

It should be emphasized then that since DM BHs can exhibit features associated with Kerr NSs, it has implications on cosmic censorship owing to the fact that observing a compact object with such tracers (excretion cusp, double cusps, double tori) would not require the breaking of cosmic censorship (viewing a Kerr NSs), but instead could mean that one is observing a BH surrounded by DM. Finally, in this work we developed a comparative analysis of accretion disks in different dark matter models, while we have reserved the in-depth explorations of different DM parametric values for future analysis.

[22]Thereby producing a so-called spike phenomenon [78].

[23]Configurations considered here have often been adopted as the initial conditions in the setup for simulations of the general relativistic magnetohydrodynamic (GRMHD) accretion structures [53–55,79]. The geometrically thick axial symmetric hydrodynamical models are widely adopted in many contexts, showing a remarkably good fitting to the more complex dynamical models, as discussed, for example, in [51]. In current analyses of dynamical systems of both GRHD and GRMHD setup, these tori are commonly adopted as initial configurations for the numerical analysis [54,55,80], which also constitutes a comparative model in many numerical analyses of complex situations sharing the same symmetries. Indeed, the general relativistic thick torus morphological features, which are related to the equilibrium (quiescent) and accretion phases as the cusp emergence, are predominantly determined by the centrifugal and gravitational components of the force balance in the disks rather then the dissipative ones.

[24]A further relevant issue in the analysis of the DM effects on BHs accretion is whether the features shown to track the DM presence may be used to distinguish between the DM models. An answer to this question comes immediately from a comparison of the horizon structures for the PFDM model in Fig. 2, the SFDM model in Fig. 9, and the CDM model in Fig. 13, and of the geodesic structure (constraining the torus morphology and formation) for the PFDM model in Fig. 3, the SFDM model in Fig. 10, and the CDM model in Fig. 14. Thus, it is immediately determined that, in general, the main differences are between the PFDM model on the one hand and the CDM and SFDM models on the other, including for small values of DM parameters. In these DM models we have pointed out DM-induced NSs (slower spinning attractors without BH horizons) and in all cases also DM-induced BHs (overspinning solutions with one or two horizons). Here we take into account DM model differentiation by means of the torus characteristics possibly determining the DM presence, as the interdisk cusps, double accretion tori, the presence of extremely large and far tori, limited protojet ranges, DM differentiation according to the fluid rotation orientation, and Lense-Thirring effects in the presence of DM. While the SFDM and CDM models show qualitatively similar characteristics in that they do not substantially distinguish among DM effects for fluid rotation orientation and slowly spinning from faster spinning attractors, the situation for PFDM is clearly different. The PFDM model also shows remarkable differences for a small variation of the DM k parameter while distinguishing among DM effects on corotating and counterrotating fluids and between slowing spinning attractors and faster spinning attractors. The CDM and SFDM models show for the considered parameters ranges ($a \in [0, M]$) a geodesics structure that is qualitatively similar to the BH case in the absence of DM. There are very large tori located far from the attractor, and protojet cusps constrained in a narrow orbital range around the attractor, constraining protojet emission and the formation of tori with large angular momenta in magnitude. We have also noticed indications of a possible alteration of the Lense-Thirring effects on the disks and flows with respect to the Kerr case without DM. In the considered parameter ranges, major differences among the PFDM models with respect to the case in which DM is absent appear in the formation of the intercusps, double configurations, and possible excretion tori. It must be stressed, however, that, while we have drawn a DM model comparative analysis here, an in-depth exploration of more extensive DM parameter ranges in all models would further narrow the DM parameters due to the DM effects on the BH accretion.

[1] P. E. Mancera Piña, F. Fraternali, T. Oosterloo, E. A. K. Adams, K. A. Oman, and L. Leisman, Mon. Not. R. Astron. Soc. **512**, 3230 (2022).
[2] P. E. Mancera Pina *et al.*, Astrophys. J. Lett. **883**, L33 (2019).
[3] E. Belbruno and J. Green, Mon. Not. R. Astron. Soc. **510**, 5154 (2022).
[4] X. Hou, Z. Xu, and J. Wang, J. Cosmol. Astropart. Phys. 12 (2018) 004.
[5] F. Rahaman, K. K. Nandi, A. Bhadra, M. Kalam, and K. Chakraborty, Phys. Lett. B **694**, 10 (2010).
[6] Z. Xu, X. Hou, and J. Wang, Classical Quantum Gravity **35**, 115003 (2018).
[7] A. Das, A. Saha, and S. Gangopadhyay, Classical Quantum Gravity **38**, 065015 (2021).
[8] Z. Xu, X. Hou, X. Gonga, and J. Wanga, J. Cosmol. Astropart. Phys. 09 (2018) 038.
[9] X. Hou, Z. Xu, M. Zhou, and J. Wang, J. Cosmol. Astropart. Phys. 07 (2018) 015.
[10] S. Shaymatov, D. Malafarina, and B. Ahmedov, Phys. Dark Universe **34**, 100891 (2021).
[11] Z. Stuchlik, Bull. Astron. Inst. Czech. **34**, 129 (1983).
[12] Z. Stuchlík and S. Hledík, Phys. Rev. D **60**, 044006 (1999).
[13] Z. Stuchlík, M. Kološ, J. Kovář, P. Slaný, and A. Tursunov, Universe **6**, 26 (2020).
[14] Z. Stuchlík and S. Hledík, Classical Quantum Gravity **17**, 4541 (2000).
[15] Z. Stuchlík, Mod. Phys. Lett. A **20**, 561 (2005).
[16] M. Khodadi and R. Pourkhodabakhshi, Phys. Lett. B **823**, 136775 (2021).
[17] B. Toshmatov, Z. Stuchlik, and B. Ahmedov, Eur. Phys. J. Plus **132**, 98 (2017).
[18] H. Kim, B. Lee, W. Lee, and Y. Lee, Phys. Rev. D **101**, 064067 (2020).
[19] B. Cuadros-Melgar, R. D. B. Fontana, and J. de Oliveira, Phys. Rev. D **104**, 104039 (2021).
[20] M. Li and K. Yang, Phys. Rev. D **86**, 123015 (2012).
[21] Z. Stuchlík and J. Schee, Classical Quantum Gravity **30**, 075012 (2013).
[22] Z. Stuchlik, Bull. Astron. Inst. Czech. **31**, 129 (1980).
[23] M. Blaschke and Z. Stuchlík, Phys. Rev. D **94**, 086006 (2016).
[24] Z. Stuchlík, S. Hledík, and K. Truparová, Classical Quantum Gravity **28**, 155017 (2011).
[25] D. Traykova, K. Clough, T. Helfer, E. Berti, P. G. Ferreira, and L. Hui, Phys. Rev. D **104**, 103014 (2021).
[26] K. Clough, P. G. Ferreira, and M. Lagos, Phys. Rev. D **100**, 063014 (2019).
[27] J. Bamber, K. Clough, P. G. Ferreira, L. Hui, and M. Lagos, Phys. Rev. D **103**, 044059 (2021).
[28] H. Davoudias, P. B. Denton, and J. Gehrlein, Phys. Rev. Lett. **128**, 081101 (2022).
[29] L. E. Padilla, T. Rindler-Daller, P. R. Shapiro, T. Matos, and J. A. Vázquez, Phys. Rev. D **103**, 063012 (2021).
[30] J. Bamber, K. Clough, P. G. Ferreira, L. Hui, and M. Lagos, Phys. Rev. D **103**, 044059 (2021).
[31] K. Jusufi, Phys. Rev. D **101**, 084055 (2020).
[32] T. Lacroix, M. Karami, A. E. Broderick, J. Silk, and C. Boehm, Phys. Rev. D **96**, 063008 (2017).
[33] K. Jusufi, M. Jamil, P. Salucci, T. Zhu, and S. Haroon, Phys. Rev. D **100**, 044012 (2019).
[34] K. Jusufi, M. Jamil, and T. Zhu, Eur. Phys. J. C **80**, 354 (2020).
[35] F. Atamurotov, U. Papnoi, and K. Jusufi, Classical Quantum Gravity **39**, 025014 (2022).
[36] R. Abbott *et al.*, Phys. Rev. D **105**, 102001 (2022).
[37] A. Das, S. A. R. Ellis, P. C. Schuster, and K. Zhou, Phys. Rev. Lett. **128**, 021101 (2022).
[38] T. S. Li, A. P. Ji, A. B. Pace *et al.*, Astrophys. J. **928**, 30 (2022).
[39] R. P. Naidu, C. Conroy, A. Bonaca *et al.*, Astrophys. J. **923**, 92 (2021).
[40] N. Cappelluti, G. Hasinger, and P. Natarajan, Astrophys. J. **926**, 205 (2022).
[41] S. Basak, A. Ganguly, K. Haris, S. Kapadia, A. K. Mehta, and P. Ajith, Astrophys. J. Lett. **926**, L28 (2022).
[42] C. Smorra, Y. V. Stadnik, and P. E. Blessing *et al.*, Nature (London) **575**, 310 (2019).
[43] S. Afach, B. C. Buchler, D. Budker *et al.*, Nat. Phys. **17**, 1396 (2021).
[44] A. Gomez-Valent, Z. Zheng, L. Amendola, V. Pettorino, and C. Wetterich, Phys. Rev. D **104**, 083536 (2021).
[45] Z. Stuchlí, S. Hledík, and J. Novotný, Phys. Rev. D **94**, 103513 (2016).
[46] M. A. Abramowicz, M. Jaroszyński, and M. Sikora, Astron. Astrophys. **63**, 221 (1978).
[47] M. Jaroszynski, M. A. Abramowicz, and B. Paczynski, Acta Astronomica **30**, 1 (1980).
[48] D. Pugliese, G. Montani, and M. G. Bernardini, Mon. Not. R. Astron. Soc. **428**, 952 (2013).
[49] D. Pugliese and G. Montani, Europhys. Lett. **101**, 19001 (2013).
[50] M. Kozłowski, M. Jaroszyński, and M. A. Abramowicz, Astron. Astrophys. **63**, 209 (1998).
[51] Q. Lei, M. A. Abramowicz, P. C. Fragile *et al.*, Astron. Astrophys. **498**, 471 (2008).
[52] M. A. Abramowicz, ASP Conf. Ser. **403**, 29 (2009).
[53] I. V. Igumenshchev and M. A. Abramowicz, Astrophys. J. Suppl. Ser. **130**, 463 (2000).
[54] P. C. Fragile, O. M. Blaes, P. Anninos, and J. D. Salmonson, Astrophys. J. **668**, 417 (2007).
[55] J-P. De Villiers and J. F. Hawley, Astrophys. J. **577**, 866 (2002).
[56] J. A. Font and F. Daigne, Astrophys. J. **581**, L23 (2002).
[57] M. A. Abramowicz and P. C. Fragile, Living Rev. Relativity **16**, 1 (2013).
[58] D. Pugliese and G. Montani, Phys. Rev. D **91**, 083011 (2015).
[59] B. Paczyński, Acta Astronomica **30**, 347 (1980).
[60] J. A. Font, Living Rev. Relativity **6**, 4 (2003).
[61] M. A. Abramowicz, M. Calvani, and L. Nobili, Astrophys. J. **242**, 772 (1980).
[62] M. A. Abramowicz, Publ. Astron. Soc. Jpn. **37**, 727 (1985).
[63] D. Pugliese and Z. Stuchlik, Eur. Phys. J. C **79**, 288 (2019).
[64] D. Pugliese and Z. Stuchlík, Classical Quantum Gravity **35**, 185008 (2018).
[65] R. H. Boyer, Proc. R. Soc. A **311**, 245 (1969).
[66] D. Pugliese and Z. Stuchlík, Astrophys. J. Suppl. Ser. **221**, 25 (2015).

[67] Z. Stuchlik, Bull. Astron. Inst. Czech. **32**, 68 (1981).
[68] D. Pugliese, H. Quevedo, and R. Ruffini, Phys. Rev. D **84**, 044030 (2011).
[69] K. Adamek and Z. Stuchlik, Classical Quantum Gravity **30**, 205007 (2013).
[70] P. Slaný and Z. Stuchlík, Classical Quantum Gravity **22**, 3623 (2005).
[71] D. Pugliese and Z. Stuchlik (unpublished).
[72] D. Pugliese and Z. Stuchlik, Mon. Not. R. Astron. Soc. **512**, 5895 (2022).
[73] D. Pugliese and Z. Stuchlík, Astrophys. J. Suppl. Ser. **223**, 27 (2016).
[74] D. Pugliese and Z. Stuchlík, Classical Quantum Gravity **35**, 105005 (2018).
[75] D. Pugliese and Z. Stuchlik, Publ. Astron. Soc. Jpn. **73**, 1333 (2021).
[76] E. Kurmanov, K. Boshkayev, R. Giambo, T. Konysbayev, O. Luongo, D. Malafarina, and H. Quevedo, Astrophys. J. **925**, 210 (2022).
[77] D. Pugliese and Z. Stuchlik, Publ. Astron. Soc. Jpn. **73**, 1497 (2021).
[78] L. Sadeghian, F. Ferrer, and C. M. Will, Phys. Rev. D **88**, 063522 (2013).
[79] R. Shafee, J. C. McKinney, R. Narayan, A. Tchekhovskoy, C. F. Gammie, and J. E. McClintock, Astrophys. J. **687**, L25 (2008).
[80] O. Porth, H. Olivares, Y. Mizuno, Z. Younsi *et al.*, Comput. Astrophys. Cosmol. **4**, 1 (2017).